In: AIAA SCITECH 2024 Forum, 8-12 January 2024, Orlando, USA, Paper number AIAA 2024-1487
DOI: 10.2514/6.2024-1487

Uncertainty propagation and management of mixed uncertainties for multi-fidelity multi-disciplinary analysis of propeller with different blade sweep

Shubham Shubham* †
Cranfield University, Bedford, MK43 0AL, United Kingdom
Nottingham Trent University, Nottingham, NG1 4FQ, United Kingdom

Timoleon Kipouros‡
Cranfield University, Bedford, MK43 0AL, United Kingdom

Siddhant Dash§
Indian Institute of Technology (BHU) Varanasi, 221005, India

Anton Ianakiev¶
Nottingham Trent University, Nottingham, NG1 4FQ, United Kingdom

A study on the uncertainty quantification and propagation in a multi-fidelity, multi-disciplinary framework, focusing on aerodynamics, aeroacoustics, and aeroelasticity in propeller blade design is presented. Employing the Lattice Boltzmann Method (LBM) for high-fidelity simulations and the Lifting Line Free Vortex Wake (LLFVW) and Finite Element Analyses (FEA) for mid-fidelity simulations, the study analyzes a 2-bladed, 0.3m diameter propeller using NACA4412 airfoil cross-section, across nine blade sweep configurations. It investigates the effects of two uncertain parameters: freestream velocity, using Interval analysis, and blade tip offset, using Monte Carlo Simulation. The differential analysis between mid and high-fidelity methods shows an uncertainty range of 13.83% to 30.32% for freestream velocity and 2% to 32.48% for blade tip offset, due to the inclusion of the mid-fidelity method. Using the Halton sampling method, it is demonstrated that the uncertainty in the sweep parameter is propagated differently across various performance metrics of the propeller. A backward sweep tends to increase both the mean (by 5-6 %) and uncertainty (by 2-4 %) in all performance parameters, suggesting a potential enhancement in performance but with increased risk. In contrast, a forward sweep reduces mean performance (by 2-3 %) and uncertainty (by 4-6 %) of all parameters except structural deflection, which shows an increasing trend (by 0.5-2 %). This indicates a more reliable aerodynamic and aeroacoustic performance but potentially less efficient operation and increased risk in structural integrity.

I. Nomenclature

D	=	propeller diameter, m
d	=	tip offset, m
r_s	=	sweep start-up point, m
R_T	=	tip radius, m
P_s	=	sweep start-up ratio
P_r	=	tip offset ratio

*Post-Doctoral Research Fellow, School of Aerospace, Transport and Manufacturing, shubham.shubham@cranfield.ac.uk, AIAA member 1345559
†PhD researcher, Sustainable Energy Systems, Department of Civil Engineering, shubham.shubham@ntu.ac.uk
‡Senior Lecturer, School of Aerospace, Transport and Manufacturing, t.kipouros@cranfield.ac.uk
§Undergraduate Student, Department of Mechanical Engineering, siddhant.dash.cd.mec20@iitbhu.ac.in
¶Professor, Sustainable Energy Systems, Department of Civil Engineering, anton.ianakiev@ntu.ac.uk

Published by AIAA. This is the Author Accepted Manuscript issued with: Creative Commons Attribution License (CC:BY 4.0).
The final published version (version of record) is available online at DOI:10.2514/6.2024-1487. Please refer to any applicable publisher terms of use.

C_T = thrust coefficient
C_Q = torque coefficient
C_P = power coefficient
f = frequency, Hz
h = grid spacing, m
M = free-stream Mach number
n = rotations per second, 1/s
Q = propeller torque, Nm
r = propeller radius, m
Re = Reynolds number
Re_c = chord-based Reynolds number
T = propeller thrust, N
V_∞ = free-stream velocity, m/s
ω = propeller rotational speed, rad/s
α = angle of attack, $^\circ$
ρ = air density, kg/m^3

II. Introduction

The aerodynamics and aeroacoustics of propellers operating at low Reynolds numbers have garnered considerable attention due to their pivotal role in various applications, such as unmanned aerial vehicles (UAVs), micro-air vehicles (MAVs), and small-scale wind turbines. These propellers are specifically designed to achieve optimal performance and efficiency at low speeds while operating within viscous fluid environments. Particularly in the case of MAVs, low Reynolds number propellers enable stable and controlled flight in cluttered surroundings, while minimizing energy consumption [1, 2]. As the demand for small-scale aerial and underwater vehicles continues to rise, the utilization of low Reynolds number propellers is expected to expand further. Consequently, comprehending the intricate aerodynamic, aeroacoustic and aeroelastic behaviour of such propellers operating at low Reynolds numbers is of utmost importance in order to enhance their performance and efficiency [3, 4]. A number of studies have been conducted on the effect of different blade shapes on such propellers and blade shape optimization.

Chang et al. [5] optimized twist distribution of propeller blades using non-linear programming. This was done for both General Aviation (GA) and Pursue Model (PM) propellers with efficiency improvement of 6% and 1%, respectively. Cho et al. [6] employed the Extended linear Interior Penalty function Method (EIPM) to optimize the propeller blade shape for efficiency improvement. The method improves the efficiency of propeller blade shapes especially when using lifting line and lifting surface methods for aerodynamic calculations and shows agreement with other numerical schemes and proves useful for validating propellers and designing high-efficiency propellers. Xia et al. [7] successfully integrated an inverse propeller design method based on the Betz optimal theory into a rapid optimization framework for a VTOL propeller. The framework considered maximum thrust-to-weight ratio at hover and mission energy as objectives, capturing both maneuverability and efficiency. The results demonstrated the advantages of a variable pitch propeller (VPP) over a fixed pitch propeller (FPP) in terms of energy savings and improved thrust-to-weight ratio at hover.

Toman et al. [8] use of two aerodynamic models, the Blade Element Momentum (BEM) theory and Computational Fluid Dynamics (CFD), to optimize propeller blade shape. The Sequential Meta-Modeling (SM) concept and Design of Experiments (DOE) algorithm with kriging response surface was employed. Although both techniques yielded similar optimum points, the SM algorithm demonstrated better computational efficiency. Wu et al. [9] showed that improved blades effectively suppress aerodynamic noise while meeting flight standards, suggesting the feasibility of reducing propeller noise by altering blade shape along the spanwise direction. Sullivan [10] studied the effect of sweep on propeller performance. Firstly, the power coefficient (C_P) decreases with sweep at a given advance ratio. Secondly, the power loading decreases in the sweep region. Thirdly, the ideal efficiency remains consistent for equal values of C_P. Additionally, the results indicate that the advance ratio for a C_P of 0 is independent of sweep, with sweep effects becoming more critical as the loading increases. Bergmann et al. [11] introduces sweep correction models for propeller analysis, including lift, drag, and tangential force corrections. The results show that turning airfoils are essential for swept propeller analysis, and up to 25% sweep, the Blade Element Theory (BET) simulations align reasonably well with RANS simulations. The Busemann lift coefficient correction significantly improves power and thrust prediction. Several other studies have been conducted on propeller sweep designs using experimental and analytical methods [12–14].

The above literature highlights that propellers with different blade shapes have been widely studied and utilized in

various applications, including large-scale aircrafts. However, their potential advantages in the context of aerial vehicles operating at low Reynolds numbers remain largely unexplored. Having a sweep along the spanwise and chordwise direction can be a potential solution to increase aerodynamic efficiency and decrease noise. To address this research gap, the current study investigates different sweep designs for a small-scale propeller operating at a low Reynolds number.

For the second part of this study, uncertainty propagation and quantification is performed using a multi-fidelity multi-disciplinary framework. The study of uncertainty propagation and quantification addresses the inherent uncertainties in material properties, manufacturing tolerances, and operational conditions, which can significantly impact the reliability and efficiency of aerospace components. The findings will provide designers and engineers with crucial information for making informed decisions during propeller design iterations, leading to improved performance, increased efficiency, and enhanced system reliability.

West et al. [15] developed a framework for multi-fidelity multi-disciplinary uncertainty quantification using a surrogate modelling approach based on the non-intrusive polynomial chaos (NIPC) using the point-collocation technique. The results are shown for a transonic airfoil model and a multidisciplinary aircraft analysis model. Chaudhuri et al. [16] introduces an innovative method that employs adaptive surrogates to minimize the need for extensive high-fidelity simulations in feedback-coupled multidisciplinary analysis under uncertainty. The proposed multi-fidelity coupled uncertainty propagation approach iteratively refines surrogate models for coupling variables using adaptive sampling strategies, ensuring accuracy in uncertainty analysis without compromising the integrity of the original high-fidelity problem. Kipouros et al. [17] presented a methodology for identifying and characterizing input uncertainties in turbomachinery design, specifically focusing on the operating conditions of gas turbine stages. The approach demonstrated through a case study on a compressor's inlet total pressure, is adaptable for various inlet and outlet conditions, aiming to achieve a robust aerodynamic design for the entire compression system of gas turbines.

In this study, two distinct numerical methods are employed: a mid-fidelity approach, represented by the Lifting Line Free Vortex Wake (LLFVW) and Finite Element Analysis (FEA) method for aerodynamics and aeroelasticity, respectively, and a high-fidelity approach utilizing the Lattice Boltzmann Method (LBM) for aerodynamics and aeroacoustics. The mid-fidelity method provides a simplified yet insightful representation of the flow field by employing vortex lifting lines. On the other hand, the high-fidelity LBM method offers a more detailed and accurate resolution of the flow characteristics, capturing the complex three-dimensional effects and unsteady phenomena. For surrogate modelling, both ordinary and multi-fidelity kriging (co-kriging) is used. Two types of uncertainties are propagated: Aleatory and Epistemic. For aleatory, Monte Carlo Simulation is used for uncertainty quantification, while for epistemic, interval analysis is employed.

The objective of this study is threefold: first, to develop a modular multi-fidelity multi-disciplinary framework for uncertainty propagation and quantification which can investigate three different disciplines - aerodynamics, aeroacoustics and aeroelasticity of any system under study. Secondly, to investigate the performance of propellers with different blade configurations of both forward and backward sweep. This includes mean performance over a single rotation and quantifying the uncertainty propagated in each discipline. Finally, to compare the capabilities of the mid-fidelity and high-fidelity methods in capturing the essential flow features and quantify the uncertainty introduced in the framework due to the usage of the mid-fidelity method. By conducting a comparative analysis, we aim to evaluate the suitability of the mid-fidelity method as a viable substitute for computationally expensive high-fidelity simulations, thereby providing a cost-effective and efficient alternative for propeller design optimization.

The paper is structured as follows. Section III discusses the methodologies used in the framework including physics-based models, surrogate modelling and uncertainty quantification methods. Section IV discusses the propeller geometries, numerical setup of the mid-fidelity and high-fidelity simulations, operational conditions and the framework developed as part of this study. Section V reports all the results obtained in this study for aerodynamics, aeroacoustics and aeroelasticity and the uncertainty propagated in each discipline. Finally, Section VI discusses the conclusions of this study and future recommendations.

III. Methodology

A. Physics-based models

1. Flow solver: mid-fidelity

The lifting line method is used to compute the force and flow field because it was shown to be accurate and efficient for similar low Reynolds number rotor applications [18–20]. The lifting line method belongs to a family of various

"vortex methods", the computational cost of which falls somewhere in between low-fidelity momentum methods (BEMT, DMS, etc.) and high-fidelity CFD methods (Navier Stokes, Lattice-Boltzmann). In the present study, the lifting line theory coupled to a free vortex wake model is used to calculate the VAWT three-dimensional (3D) unsteady flow field past the rotor and the interaction between blade and fluid flow [21, 22]. The LLFVW algorithm is based on nonlinear lifting line formulation by Garrel [23] and is mentioned in detail by Balduzzi [22].

The fluid is modelled as incompressible, inviscid and irrotational; the blade is modelled with a single line of vortices which is located on the quarter chord points of the blade. The wake is discretised into vortex line elements (straight or curved) and these elements are shed at the blade trailing edges at every time step. They then undergo free convection past the rotor ("free wake method") in which the position of the wake end nodes is updated based on the local velocity, which is a combination of inflow velocity and induced velocity from all the wake elements in the domain. Nonlinear in the "nonlinear lifting line formulation" means the circulation calculated on the lifting line bound vortices is acquired from the nonlinear airfoil lift and drag data provided as input. Lift and drag forces are then calculated based on the local angle of attack (α).

The vortex elements are desingularised using the van Garrel's cut-off method [24] with the vortex core size, taking into account viscous diffusion via the vortex core size that is modelled through the kinematic viscosity ν, a turbulent vortex viscosity coefficient δ_v, and a time offset parameter S_c using the below equation:

$$r_c = \left(\frac{5.03 \delta_v \nu \, (t + S_c)}{1 + \varepsilon} \right)^{1/2} \tag{1}$$

The effects of unsteady aerodynamics and dynamic stall are introduced via the ATEFlap aerodynamic model [25, 26] that reconstructs lift and drag hysteresis curves from a decomposition of the lift polars. The implemented ATEFlap formulation has been further adapted to work under the complex conditions of VAWT exhibiting large fluctuations in the angle of attack when rotating at low TSR [27]. Wake reduction schemes have been implemented to lower computational requirements [25–28]. In the present study, all results with this method will henceforth be referred to with the 'LLFVW' nomenclature.

2. Flow solver: high-fidelity

The Lattice Boltzmann Method (LBM) is used to compute the flow field because it was shown to be accurate and efficient for similar low Reynolds number rotor applications [18, 29–31]. The commercial software 3DS Simulia PowerFLOW has been already validated for aerodynamic and aeroacoustic studies on rotors in general [32–34]. The software solves the discrete Lattice Boltzmann (LB) equation for a finite number of directions. For a detailed description of the method, the reader can refer to Succi [35] and Shan et al. [36], while to Chen and Doolen [37] for a review. The LB method determines the macroscopic flow variables starting from the mesoscopic kinetic equation, i.e. the LB equation. The discretization used for this particular application consists of 19 discrete velocities in three dimensions (D3Q19), involving a third-order truncation of the Chapman-Enskog expansion [38]. The distribution of particles is solved by means of the LB equation on a Cartesian mesh, known as a lattice. An explicit time integration and a collision model are used. For the collision term, the formulation based on a unique Galilean invariant [39] is used. The equilibrium distribution of Maxwell-Boltzmann is adopted [38].

To take into account the effect of the sub-grid unresolved scales of turbulence, a Very Large Eddy Simulation (VLES) model is implemented. Following Yakhot and Orszag [40], a two-equations $k - \epsilon$ Renormalization Group is used to compute a turbulent relaxation time that is added to the viscous relaxation time. To reduce the computational cost, a pressure-gradient-extended wall-model is used to approximate the no-slip boundary condition on solid walls [41, 42]. The model is based on the extension of the generalised law-of-the-wall model [43] to take into account the effect of pressure gradient. These equations are iteratively solved from the first cell close to the wall in order to specify the boundary conditions of the turbulence model. For this purpose, a slip algorithm [37], obtained as generalization of a bounce-back and specular reflection process, is used.

3. Structural solver: mid-fidelity

The structural analysis within QBlade uses the finite element analysis (FEA) capabilities of the open-source multi-physics engine, Project Chrono [44]. Project Chrono is a platform-independent design [45] and is developed as an object-oriented library in the C++ programming language. For the integration, the Chrono::Engine module is utilized which is the core module of Project::Chrono. This module facilitates the construction and resolution of physical systems

characterized by Newtonian dynamics and finite element methodologies. The finite element problems are solved using the SparseLU solver from the EIGEN C++ template library [46].

The structural model for propellers in the QBlade-Chrono coupling interface is composed of Euler-Bernoulli beams, which are articulated within a co-rotational framework [47]. A floating (local) coordinate system is affixed to each deformable beam element, allowing for the decomposition of the beam's motion into rigid-body movements (translations and rotations) of the floating frame and smaller strain deformations, which are quantified relative to this floating reference frame. Project Chrono's formulation of the global tangent stiffness matrix incorporates components that account for geometric stiffness. The aerodynamic and geometric parameters specified by the user are automatically processed to extract the structural discretization of the propeller blades. The rotor's geometry is not only defined aerodynamically but also through its sectional mass and stiffness characteristics, which inform the construction of the structural entities. Based on the structural and geometrical properties, these entities are subsequently interconnected through constraints to form the complete structural model. The cross-sectional properties of each structural body are defined [48], including the Centre of Mass, Shear Center, Elastic Center, Principal Bending Axes, Structural Pitch, among others [164].

4. Aeroacoustic coupling: high-fidelity

Aeroacoustic coupling within the PowerFLOW framework is set up with a *tight coupling* scheme, which means the time integration is carried out over the complete system [49] involving all the different simulation models, in this case, which is the aerodynamic solver and sampling of pressure fluctuations for aeroacoustic post-processing on FW-H surfaces. Effectively this means that the sub-simulations (aerodynamics and acoustics) exchange their information during the iteration procedure or the setup of the system of equations and requires all sub-simulations to advance at an equal time step.

Far-field noise is computed using the Ffowcs Williams and Hawkings [50] (FW-H) acoustic analogy. In particular, the formulation 1A of Farassat and Succi [51] extended to a convective wave equation is used in this study [52]. The formulation has been implemented in the time domain using a source-time dominant algorithm [53]. Pressure fluctuations are recorded on three permeable surfaces enclosing the wind turbine and its wake. These pressure fluctuations are used as input to the FW-H solver, thereby including all noise sources inside the three surfaces. Pressure fluctuations are also captured on all solid surfaces (blade surfaces), which when input to the FW-H solver will include noise sources only on the solid surfaces.

5. Aeroelastic coupling: mid-fidelity

Aeroelastic simulations within this study are conducted using a *loose coupling* scheme, wherein distinct sub-simulations are executed independently and subsequently integrated. The loose coupling approach is utilized for the co-simulation using the aerodynamic and structural dynamics models. Typically, the LLFVW aerodynamic simulation progresses through time steps corresponding to 5° to 10° of rotor rotation. Although the structural model is capable of stable computations with larger time steps, the integration with the supervisory controller, the associated actuators, and their respective actuation ranges and frequencies, necessitates finer time steps for accurate structural simulation [48]. The algorithm for one complete aeroelastic simulation time step is comprehensively explained by Marten [48].

B. Surrogate modelling

The surrogate modelling approach used in this study has its origins derived from the popular surrogate modelling approach - Kriging. The next few sections explain the methodology implemented in detail.

1. Ordinary Kriging

The Kriging model assumes that points within proximity to each other within a design domain exhibit similar functional values. Within a d-dimensional hypercube, the correlation amongst points is assumed to follow the relationship given by [54]:

$$\boldsymbol{R}_{ij} = \exp\left(-\sum_{l=1}^{d} 10^{\boldsymbol{\theta}^{(l)}} \left\|\boldsymbol{x}_i^{(l)} - \boldsymbol{x}_j^{(l)}\right\|^{\boldsymbol{p}^{(l)}}\right), \tag{2}$$

where θ characterizes the correlation decay rate and p describes the 'smoothness' of the model across each dimension. These parameters, together with a regularization term, 10_λ, which is incorporated into the correlation matrix diagonal

[55], can be calculated through the optimization of the concentrated log-likelihood function [56]:

$$\phi = -\frac{n}{2}\ln\left(\hat{\sigma}^2\right) - \frac{1}{2}\ln(|\boldsymbol{R}|). \tag{3}$$

The variance is defined by:

$$\hat{\sigma}^2 = \frac{1}{n}(\boldsymbol{y} - \mathbf{1}\hat{\mu})^T \boldsymbol{R}^{-1}(\boldsymbol{y} - \mathbf{1}\hat{\mu}), \tag{4}$$

while the mean of the observations is given by:

$$\hat{\mu} = \frac{\mathbf{1}^T \boldsymbol{R}^{-1}\boldsymbol{y}}{\mathbf{1}^T \boldsymbol{R}^{-1}\mathbf{1}}, \tag{5}$$

where, $\mathbf{1}$ represents an n-dimensional vector of ones, and n equates to the quantity of data points within the sampling framework which is the foundation of the model architecture. Once the hyperparameters are established, the model's predictor

$$y\left(\boldsymbol{x}^*\right) = \hat{\mu} + \boldsymbol{r}^T \boldsymbol{R}^{-1}(\boldsymbol{y} - \mathbf{1}\hat{\mu}), \tag{6}$$

yields the estimated output at an unsampled location within the design space.

The optimization of hyperparameters constitutes a critical step in the development of Kriging models, significantly influencing the accuracy of the resultant model. However, the computational expense associated with inverting the correlation matrix $\mathbf{R}$, which scales in a cubic manner with the number of data points $O(n^3)$, becomes substantial for an extensive training dataset. To mitigate this computational demand and expedite the optimization process, Toal et al. [57] introduced an adjoint-based approach to the likelihood function, enabling efficient computation of the function's derivatives with respect to each hyperparameter. Utilizing the collection of adjoints provided by Giles [58], the adjoint of the correlation matrix $\mathbf{R}$ is expressed as:

$$\overline{\boldsymbol{R}} = \frac{1}{2\hat{\sigma}^2}\boldsymbol{R}^{-T}(\boldsymbol{y} - \mathbf{1}\hat{\mu})^T(\boldsymbol{y} - \mathbf{1}\hat{\mu})^T\boldsymbol{R}^{-T} - \frac{1}{2}\boldsymbol{R}^{-T}. \tag{7}$$

The derivatives of the log-likelihood function relative to θ are given as:

$$\frac{\partial\phi}{\partial\theta_l} = \ln 10 \sum_{ij} -10^{\theta_l}\left\|\boldsymbol{x}_{i_l} - \boldsymbol{x}_{j_l}\right\|^{p_l}\boldsymbol{R}_{ij}\overline{\boldsymbol{R}}_{ij}, \tag{8}$$

and relative to p are given as:

$$\frac{\partial\phi}{\partial p_l} = \sum_{ij} -10^{\theta_l}\left\|\boldsymbol{x}_{i_l} - \boldsymbol{x}_{j_l}\right\|^{p_l}\ln\left\|\boldsymbol{x}_{i_l} - \boldsymbol{x}_{j_l}\right\|\boldsymbol{R}_{ij}\overline{\boldsymbol{R}}_{ij}. \tag{9}$$

Should a regularization term be incorporated to account for noise in the training data, its derivative can also be calculated as:

$$\frac{\partial\phi}{\partial\lambda} = 10^{\lambda}\ln 10\sum_{i}\overline{\boldsymbol{R}}_{ii}. \tag{10}$$

To address the optimization challenge of hyperparameters, the hybridized particle swarm optimization algorithm proposed by Toal et al. [59] is implemented. This algorithm, an adaptation of the particle swarm technique originally formulated by Eberhart et al. [60], implements a particle initialization strategy based on an optimal Latin hypercube. A rank-based selection mechanism is employed to select a particle for localized improvement through sequential quadratic programming (SQP) in each generation (iteration).

2. Multi-Fidelity Kriging

Multi-fidelity Kriging (MFK), an extension of Ordinary Kriging, employs the autoregressive methodology proposed by Kennedy et al. [61] to integrate simulations of varying computational costs. This approach assumes that the output from a high-fidelity, computationally expensive simulation ($Z_e(x)$) can be modelled as a linear combination of a scaled low-fidelity, less expensive simulation ($Z_c(x)$) and an additional term representing the discrepancy between the two ($Z_d(x)$), mathematically represented as:

$$Z_e(\boldsymbol{x}) = \rho Z_c(\boldsymbol{x}) + Z_d(\boldsymbol{x}). \tag{11}$$

In this equation, ρ signifies a scaling factor determined during the optimization of hyperparameters. The subscripts c, e, and d denote the inexpensive (low-fidelity), expensive (high-fidelity), and the difference between inexpensive and expensive components, respectively. The correlation matrix for a multi-fidelity Kriging model is defined as:

$$\boldsymbol{C} = \begin{pmatrix} \sigma_c^2 \boldsymbol{R}_c\left(\boldsymbol{X}_c, \boldsymbol{X}_c\right) & \rho\sigma_c^2 \boldsymbol{R}_c\left(\boldsymbol{X}_c, \boldsymbol{X}_e\right) \\ \rho\sigma_c^2 \boldsymbol{R}_c\left(\boldsymbol{X}_e, \boldsymbol{X}_c\right) & \rho^2\sigma_c^2 \boldsymbol{R}_c\left(\boldsymbol{X}_e, \boldsymbol{X}_e\right) + \sigma_d^2 \boldsymbol{R}_d\left(\boldsymbol{X}_e, \boldsymbol{X}_e\right) \end{pmatrix}, \tag{12}$$

where $\boldsymbol{R}_c\left(\boldsymbol{X}_c, \boldsymbol{X}_c\right)$ defines the correlation matrix for the low-fidelity data points, and $\boldsymbol{R}_c\left(\boldsymbol{X}_c, \boldsymbol{X}_e\right)$ defines the correlation between the high-fidelity and low-fidelity data points, both utilizing the hyperparameters derived from the low-fidelity Kriging model. Conversely, $\boldsymbol{R}_d\left(\boldsymbol{X}_e, \boldsymbol{X}_e\right)$ specifies the correlation matrix for the high-fidelity data points, based on the hyperparameters from the difference model. The correlation in each instance adheres to the relationship established in Eq. 2.

The development of a multi-fidelity model proceeds in two steps. Initially, an Ordinary Kriging model is constructed using solely the low-fidelity data, with hyperparameters optimized through the maximization of the likelihood function. Subsequently, a second Ordinary Kriging model is formulated to estimate the difference between the low- and high-fidelity data. This process involves the computation of a vector of differences, denoted as $\mathbf{d}$, between the two sets of data:

$$\boldsymbol{d} = \boldsymbol{y}_e - \rho \boldsymbol{y}_c(\boldsymbol{X}_e). \tag{13}$$

The formulation of the difference model within a multi-fidelity Kriging framework mirrors the construction of an Ordinary Kriging model, with the addition of optimizing the hyperparameter ρ alongside the usual parameters θ and p. This optimization is accelerated by the adjoint-based approach described in Equations 8 and 9. The derivative of the likelihood function with respect to ρ is computed as:

$$\frac{\partial \phi}{\partial \rho} = -\sum_{i=1}^{n_e} \boldsymbol{y}_{c_i} \overline{\boldsymbol{d}}_i, \tag{14}$$

utilizing the adjoint of the difference vector which is given by Toal et al. [59]:

$$\bar{\mathbf{d}} = -\mathbf{R}_d^{-1}\left(\mathbf{d} - \mathbf{1}\hat{\mu}_d\right)\left(\frac{1}{\hat{\sigma}_d^2}\right). \tag{15}$$

In this context, σ_d^2 represents the variance within the difference model, computed using Equation 4, where the variables $\mathbf{y}$, $\mathbf{R}$, and $\hat{\mu}$ are substituted by $\mathbf{d}$, $\mathbf{R}_d$, and $\hat{\mu}_d$ respectively.

Once the hyperparameters are determined, the model is capable of predicting the response of the high-fidelity function at an unknown point $\mathbf{x}^*$, as given by:

$$y_e\left(\boldsymbol{x}^*\right) = \hat{\mu} + \boldsymbol{c}^T \boldsymbol{C}^{-1}(\boldsymbol{y} - \mathbf{1}\hat{\mu}), \tag{16}$$

and the mean is given by:

$$\hat{\mu} = \frac{\mathbf{1}^T \boldsymbol{C}^{-1} \boldsymbol{Y}}{\mathbf{1}^T \boldsymbol{C}^{-1} \mathbf{1}}, \tag{17}$$

and the vector of correlations is:

$$\boldsymbol{c} = \begin{bmatrix} \rho\hat{\sigma}_c^2 \boldsymbol{R}_c\left(\boldsymbol{X}_c, \boldsymbol{x}^*\right) \\ \rho^2\hat{\sigma}_c^2 \boldsymbol{R}_c\left(\boldsymbol{X}_e, \boldsymbol{x}^*\right) + \hat{\sigma}_d^2 \boldsymbol{R}_d\left(\boldsymbol{X}_e, \boldsymbol{x}^*\right) \end{bmatrix}. \tag{18}$$

$\mathbf{Y}$ denotes a single vector combining both inexpensive (low-fidelity) and expensive (high-fidelity) observations: $[\boldsymbol{y}_c, \boldsymbol{y}_e]$.

C. Uncertainty quantification

The next few sections describe the uncertainty quantification (UQ) methodology used in this study, the uncertainty sampling method Monte Carlo Simulation (MCS). Each technique is studied alongside different types of uncertainties — aleatory, stemming from inherent variability, and epistemic, arising from limited knowledge — which collectively shape the fidelity of predictive models.

1. Monte Carlo Simulation (MCS)

For uncertainty quantification and propagation of uncertainties within a model, the Monte Carlo Simulation (MCS) is the most common technique used [62]. It is known for its non-intrusive properties and is extensively employed in the domains of uncertainty quantification, design optimization, and analytical studies [63, 64] and has advantages over alternative uncertainty quantification techniques, such as generalized Polynomial Chaos (gPC) [65]. The non-intrusive behaviour means not requiring the implementation of a new simulation code to simulate a stochastic model. Existing deterministic simulation programs can be repurposed for stochastic analyses by iteratively executing the code with varied sets of randomly generated parameters.

MCS method generates multiple realizations or *samples* of random parameters, each according to their respective probabilistic distribution or *stochastic model*. Each sample defines a deterministic problem, which is solved (*processing*) using a deterministic solver, thereby yielding a dataset. Subsequently, statistical analysis is applied to this collective dataset to determine the response characteristics of the system under examination [66–68]. A general MC algorithm [69] is depicted in Figure. The unbiased nature of MCS across varying levels of accuracy renders it a good benchmark for evaluating the performance of alternative methodologies. For eg. the uncertainty analysis via MCS is generally discussed through the calculation of the first moment, namely the mean. However, this single metric may not always adequately represent the overall structure of the output distribution. The mean is computed using:

$$\pi = E[f(\mathbf{x})] = \int f(\mathbf{x}) p(\mathbf{x}) d\mathbf{x}, \tag{19}$$

where $f(\mathbf{x})$ represents any given output function and $p(\mathbf{x})$ denotes the probability distribution function of the random variable $\mathbf{x}$. The computation of π is rarely feasible through analytical methods, as the functions $f(\mathbf{x})$ and $p(\mathbf{x})$ can rarely be explicitly defined, and the integration domain is often complex. The simplest MCS methodology involves direct sampling from the probability distribution of $\mathbf{x}$. An empirical estimate of the statistics π, based on perfect Monte Carlo sampling is [70]:

$$\widehat{\pi} = \frac{1}{N} \sum_{i=1}^{N} w_i f\left(X^{(i)}\right), \tag{20}$$

where N independent distributed random samples $\left\{X^{(i)}; i = 1, \ldots, N\right\}$, each with associated quadrature weights $\{w_i; i = 1, \ldots, N\}$. 'Almost sure convergence' is achieved as $N \to \infty$. While Gaussian quadrature [71] and other quadrature or cubature methods [72, 73] are aligned with this approximation strategy, they are less favoured due to the exponential increase in computational expense with higher dimensions. Alternative approximation techniques, such as sensitivity-based methods [74] including first-order first-moment (FOFM), first-order second-moment (FOSM), and second-order first-moment (SOFM), utilize low-order Taylor series for numerical integration. These approximation strategies, along with variance reduction techniques, are exhaustively discussed in [75].

The drawback of MCS lies in its computational expense; extensive simulations can become impractical when individual realizations are time-consuming or when the sample size required for accurate results is prohibitively large [66–68].

2. Types of Uncertainties in Numerical Simulations

There are three distinct categories of uncertainty and error within numerical simulations [76]: aleatory uncertainty, epistemic uncertainty, and numerical error. Aleatory uncertainty arises from the intrinsic variability inherent to physical systems, attributable to the stochastic nature of input data. This type of uncertainty is quantifiable through probability density functions, provided there is ample experimental data to estimate the distribution, such as uniform or normal

distributions. Examples of aleatory uncertainty in stochastic external aerodynamics include variations in free-stream velocity or manufacturing discrepancies. It is often termed *irreducible* uncertainty due to its inherent randomness.

Epistemic uncertainty arises from a lack of knowledge, incomplete information, or ignorance regarding certain aspects of the system under study. This could include, for instance, unknown transport quantities in high-temperature hypersonic flow simulations or unknown properties of materials in the future design of propellers. This form of uncertainty is fundamentally attributed to the partial understanding of the system's characteristics. Consequently, the increase of knowledge about the system can mitigate epistemic uncertainty, rendering it a *reducible* form of uncertainty. Oberkampf et al. [77] have demonstrated that the application of probabilistic models to characterize epistemic uncertainties may result in inaccurate estimations of uncertainty levels within response predictions. This inaccuracy stems from an insufficient understanding of the probabilistic nature of the uncertainties in question. Interval analysis, which utilizes upper and lower bounds determined by limited data or expert opinion, is one method to address epistemic uncertainties. The current study deals with both kinds of uncertainties: aleatory and epistemic, for a propeller.

Numerical error, distinct from the aforementioned uncertainties, refers to identifiable shortcomings in the modelling and simulation processes that are not a result of knowledge gaps. Such errors, if not well-characterized, are considered a component of epistemic uncertainties. An example of numerical error is the discretization error that occurs in the spatial or temporal domains due to the numerical solution of partial differential equations, which govern the physical models in computational meshes.

IV. Numerical setup

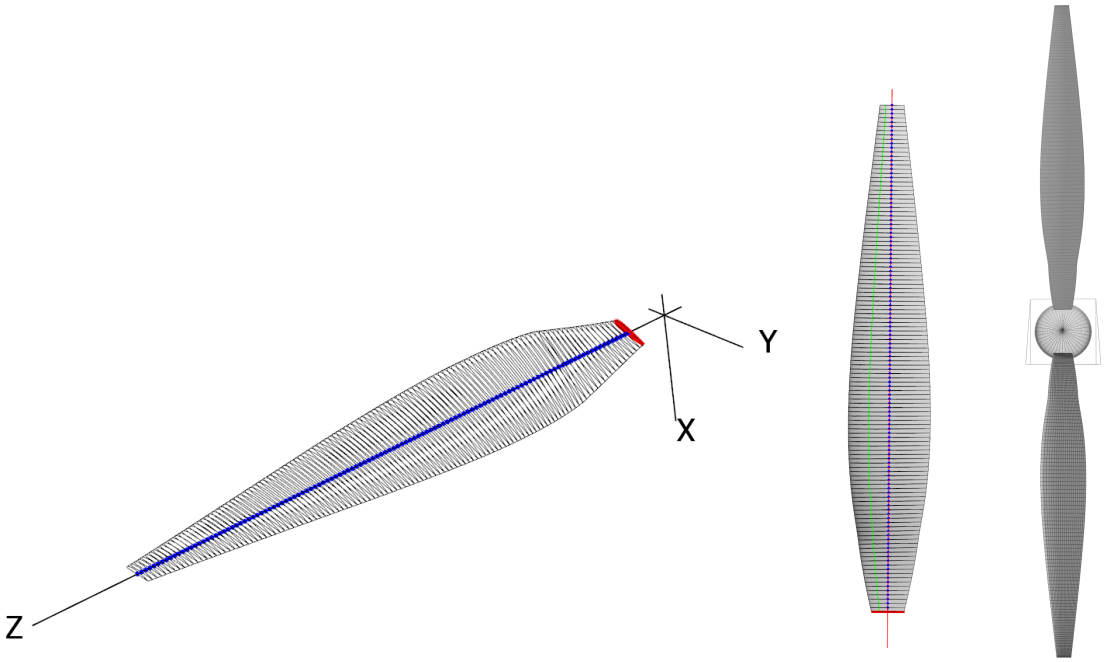
A. Propeller geometry

The baseline propeller geometry used is a two-bladed rotor and employs the NACA4412 airfoil profile throughout the blade span starting from 0.2 to 1 r/R, which is consistent with the propeller geometry used in Casalino et al. [78]. The blade geometry is made up of 120 blade sections with varying twist and chord lengths as shown in Fig. 1. The variations in chord length and twist of the airfoil sections with radial distance are extracted from the chord and twist distribution data presented in Casalino et al. [78] and shown in Figure 2. The propeller has a diameter of ($D = 0.3$ m), rotor diameter (tip radius $R_T = 0.15$ m), and a root section that transitions from a NACA0012 airfoil at a radius of 1cm ($r/R_T = 6\%$). The hub radius is 1.25cm.

The swept blade geometries considered in this study are both forward and backward sweeps of the blades. The convention of forward and backward sweeps are shown in Fig. 3. The chord and twist distribution of the swept blades is the same as the baseline geometry and made up of 120 blade sections; the only difference is the location of each blade section in the Y-direction (directions shown in Fig. 1 (a)). The geometry is determined by two parameters: the sweep start-up ratio $P_s = r_s/R_T$, and the tip offset ratio $P_r = d/R_T$. Here, P_s represents the ratio of the radial distance of the sweep start-up point (r_s) to the blade radius (R_T), and P_r represents the ratio of the tip offset (d) to the blade radius (R_T). The offset of each blade section is therefore given by the equation $y = P_r \cdot r$. This shows that the higher the tip offset ratio, the higher the sweep of the blade. To investigate the effects of swept blades, eight different blade configurations are considered aside from the baseline configuration, as shown in Table 1. Positive sweep (+) is for the backward swept and negative sweep (-) is for the forward swept blades.

Table 1 Swept blade configurations and the baseline configuration

Blade	Sweep	Sweep start up ($P_s = r_s/R_T$)	Tip offset ($P_r = d/R_T$)
Sweep-4	Forward	0.35	-0.4
Sweep-3	Forward	0.35	-0.3
Sweep-2	Forward	0.35	-0.2
Sweep-1	Forward	0.35	-0.1
Sweep+0	No sweep	0.0	0.0
Sweep+1	Backward	0.35	0.1
Sweep+2	Backward	0.35	0.2
Sweep+3	Backward	0.35	0.3
Sweep+4	Backward	0.35	0.4



(a) Isometric view (b) Top view (c) 2-bladed propeller

Fig. 1 Baseline propeller geometry, referred to as Sweep+0

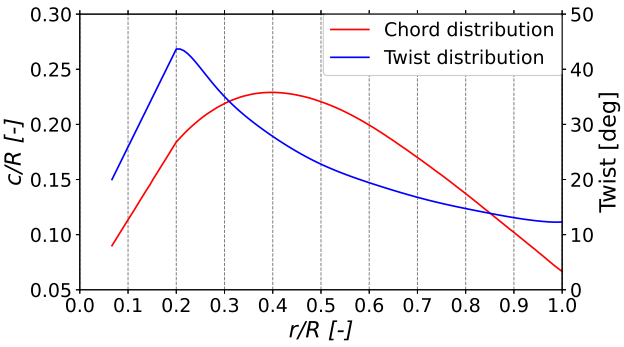
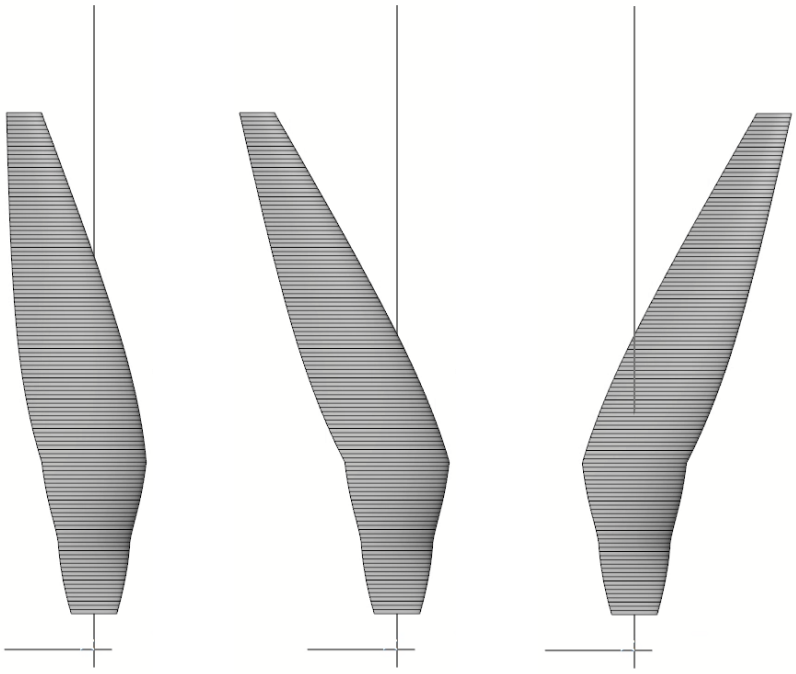


Fig. 2 Chord and twist distribution of the propeller blade

The present study utilizes high-fidelity LBM simulations for the baseline propeller geometry, forward Sweep-2 and Sweep-4, and the backward Sweep+2 and Sweep+4 configurations. In addition, the mid-fidelity LLFVW method is employed to simulate each of the nine propeller configurations. To ensure accurate results with both low and mid-fidelity methods, precise airfoil data is essential. To obtain lift and drag coefficients, XFoil [79] is employed for Reynolds numbers ranging from 1×10^5 to 5×10^6. The XFoil calculations utilize an *NCrit* value of nine and natural transition at both the pressure and suction side. The airfoil's static polar data is extrapolated to a 360° range of angle of attack (AoA) using the Montgomerie method [80] to ensure a smooth extrapolation in the post-stall regime. Balduzzi et al. [22] provide an example of the 360° extrapolated polars using the same method.

B. Computational setup

In the high-fidelity LBM approach, a simulation volume is employed, characterized as a cube with all sides measuring $100D$. This volume encompasses the propeller geometry, which is centrally positioned within the domain.



(a) Backward swept +2 (b) Backward swept +4 (c) Forward swept -4

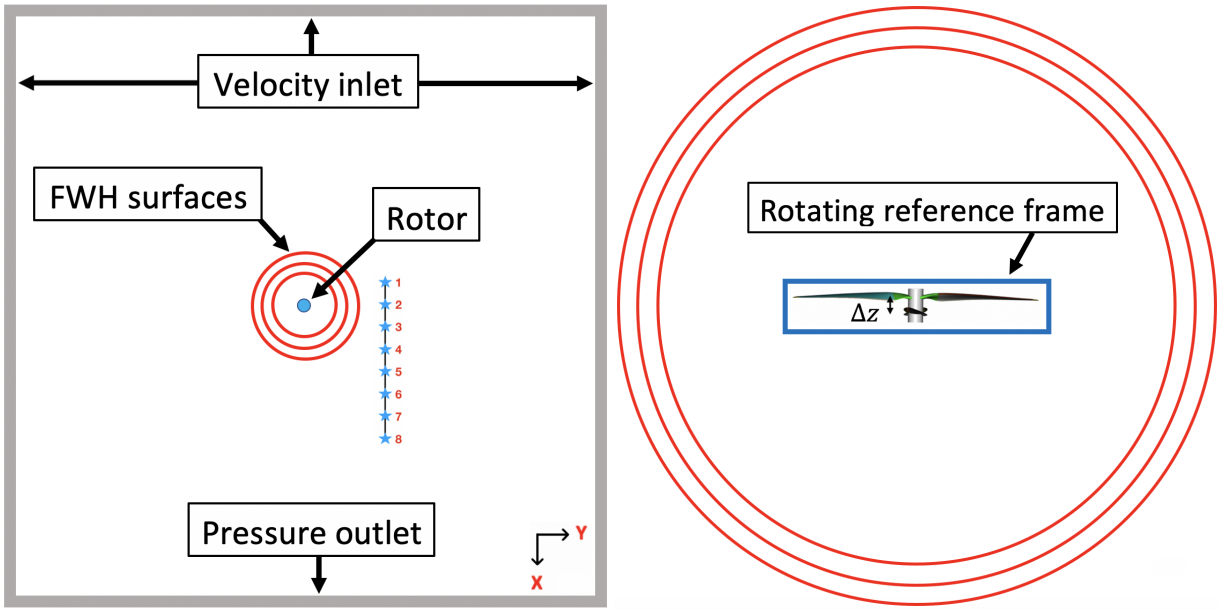
Fig. 3 Swept propeller blade geometries for three different sweep configurations; leading edge is on the right hand of each image

The corresponding boundary conditions are illustrated in Figure 4 (a). Specifically, the velocity inlet is set to the freestream velocity V_∞ along the X-axis, while a constant ambient pressure of 101.325 kPa is imposed at the pressure outlet. Additionally, the blade surface adheres to a no-slip boundary condition. To facilitate the generation of a computational grid, PowerFLOW utilizes a Cartesian volume mesh encompassing the individual solid components within the simulation domain. This process commences with the smallest hexahedral cell (voxel) size and incorporates a specified number of variable resolution (VR) levels. The VR levels are organized in a fine-to-coarse sequence, with a voxel size change factor of 2 between adjacent VRs, resulting in distinct VR regions. The software automatically intersects the Cartesian mesh with the solid components, thereby generating a collection of polygons known as surfels, which accurately represent the body's surface geometry.

In order to enhance computational efficiency, the present study employs 17 VR regions. These regions feature higher resolutions in proximity to the blade surface, incorporating an offset, while the coarser regions are positioned further away from the blade and rotor. This strategic allocation of computational effort prioritizes areas of interest and regions expected to exhibit significant flow gradients, thus optimizing the simulation process.

In Figure 4 (a) and (b), three red spherical surfaces are depicted, enclosing the rotor flow field. These surfaces serve as FW-H permeable surfaces, aimed at mitigating hydrodynamic fluctuations originating from the propeller wake vortices. By averaging the pressure data collected from these permeable surfaces, the presence of spurious noise sources can be diminished. The blade surfaces of the propeller are identified as FW-H solid surfaces. While the utilization of the FW-H permeable formulation is a potential alternative, it has not been employed in this particular study due to challenges associated with eliminating spurious noise sources solely through the use of three spherical surfaces. However, future investigations will explore a more efficient implementation of the FW-H permeable formulation for propeller aeroacoustics. To ensure accurate capture of acoustic waves, a criterion of a minimum of 15 points per wavelength is adopted, and pressure data is sampled at a frequency of 8000 Hz over eight complete rotor rotations. Subsequently, noise spectra are computed using a Hanning window with 50% overlap and a frequency resolution (Δf) of 10 Hz.

For the mid-fidelity LLFVW simulation, Table 2 outlines the values of the simulation parameters utilised, which have been adopted from a previously validated setup by Shubham et al. [18] for a similar low Re rotor application.



(a) Full computational domain

(b) Zoomed-in view near the propeller

Fig. 4 Numerical setup (adapted from Shubham et al. [30, 81])

Table 2 Simulation parameters used for the LLFVW method

	LLFVW
Freestream velocity V_∞	0 m/s
Density	1.225 kg/m^3
Kinematic viscosity	1.65 e-5 m^2/s
Blade discretization	120 (cosine)
Azimuthal discretization	3 deg
Full wake length	12
Vortex time offset	1 e-4 sec
Turbulent vortex viscosity	50

C. Flow conditions and grid settings

Table 3 presents the operational settings of the propeller in the context of both the mid-fidelity and high-fidelity methods employed in the current study. The system's operational state is characterized using the Advance Ratio (AR) as a metric. The AR is defined as the ratio of the freestream velocity to the propeller tip speed and is denoted as J: (V_∞/nD), where V_∞ represents the freestream velocity, n rotations per second and D the propeller diameter. For this investigation, two freestream velocities of 0 and 10 m/s are considered, in accordance with the conditions reported by Casalino et al. [78]. The range of 0 - 10 m/s is also within the limits of wind velocities in urban areas, which are likely to be experienced by urban air vehicles.

Both the mid-fidelity and the high-fidelity methods are used to simulate at both the freestream velocities, for the baseline configuration. The freestream turbulence intensity (I_t) and turbulence length scale (L_t) are both set to 0.1% and 1 mm, respectively. However, it is anticipated, based on prior research by Casalino et al. [33], that these parameters will not significantly influence the evolution of the unsteady flow field.

The current high-fidelity setup and grid configuration employed in this study are based on the study conducted by Casalino et al. [78]. The previous study extensively tested various grid sizes, and the chosen setup has been adopted as it has demonstrated satisfactory performance. In the finest VR, the values of y+ and voxels per chord are determined to be 30 and 2.7 $\times 10^2$, respectively. The y+ value represents a dimensionless parameter indicating the distance of the first

Table 3 Propeller operational settings for the mid-fidelity and high-fidelity method

Parameter		
Freestream velocity (V_∞)	0 m/s	10 m/s
Advance ratio (J)	0	0.4
Rotations per minute (RPM)	5000	5000
Minimum Reynolds number (Re_cmin)	4.64e4	5.63e4
Maximum Reynolds number (Re_cmax)	9.67e4	9.97e4

cell centre from the computational domain's wall in the wall-normal direction. In the present study, it is computed based on the rotational velocity experienced by the blade at the mid-span location. The voxels per chord parameter, on the other hand, signifies the number of grid cells along the chord direction of the blade and is also evaluated at the blade mid-span location. It is important to note that these grid parameters have been carefully selected and optimized to ensure accurate and efficient simulations in the current investigation, leveraging the knowledge and findings from a previous study on co-rotating propellers [30, 31].

The voxel size corresponding to the finest VR used in the baseline propeller configuration is 0.315 mm. Within the computational domain, the number of fine equivalent voxels is 30.94 million. These fine equivalent voxels are obtained by multiplying the number of voxels by the time stepping rate, which is directly linked to the mesh resolution level. Importantly, doubling the voxel size results in a computational cost reduction of half, as the time step is also doubled accordingly. For the simulations performed in this study, the computational effort is quantified in CPU hours and amounts to 2.01e04 for the simulation of 12 rotor rotations (0.144 s). The simulations were executed on a Linux workstation equipped with an AMD Ryzen Threadripper 3990X Gen3 64 Core 128GB DDR4 3GHz platform. In terms of temporal discretization, the physical time step corresponding to the grid used ensures a Courant-Friedrichs-Lewy (CFL) number of 1 in the finest VR level. Consequently, the time step values are determined to be 1.51×10^{-6} s.

D. Mixed Aleatory-Epistemic Uncertainty Propagation Framework

Fig. 5 depicts the overall framework developed as part of this study. This focuses on a Mixed Aleatory-Epistemic Uncertainty Propagation Framework within the context of multi-disciplinary, multi-fidelity analysis. This framework is designed to address the complexities and uncertainties inherent in three different disciplines (aerodynamics, aeroacoustics and aeroelasticity), particularly considering varying sweep angles and freestream velocities in the context of propeller performance.

The framework is centred around the propagation of two types of uncertainties: aleatory and epistemic. Aleatory uncertainty is quantified through the Monte Carlo Simulation (MCS) method. In this context, the sweep angle parameter is identified as an aleatory uncertain parameter, primarily due to variability introduced by different manufacturing processes. This parameter is studied utilizing a normal or Gaussian distribution. Epistemic uncertainty, on the other hand, is quantified using interval analysis, with freestream velocity as the uncertain parameter. This choice is based on the unpredictability of velocities in urban areas, particularly relevant when considering the operation of future urban air vehicles. The range and distribution of these velocities are not known a priori, making interval analysis a suitable method for quantification.

The primary focus of the framework is on understanding how these uncertainties propagate and affect key outputs in aerodynamics, aeroacoustics, and aeroelasticity. Specifically, it examines the impact on aerodynamic thrust and torque, noise production in decibels by the propeller, and the aeroelastic/structural phenomenon of bending for the blade. An important aspect of the framework is the coupling between different disciplines. Aerodynamic and aeroacoustic analyses are tightly coupled, while aerodynamic and aeroelastic analyses exhibit a loose coupling, as explained in Sections III.A.4 and III.A.5, respectively. Additionally, there is a variation in the fidelity of data available for each discipline: aerodynamics has both mid and high-fidelity data, aeroacoustics has only high-fidelity data, and aeroelasticity has only mid-fidelity data. This disparity in data fidelity introduces an inherent uncertainty, which the framework also addresses. This is being referred to here as a second-order uncertainty, encompassing both the inherent uncertainty due to fidelity variations and the propagated uncertainty from input parameters.

The framework operates in two primary steps or stages:

1) *Initial Epistemic Uncertainty Prescription*: In the first stage, an epistemic uncertain variable (freestream velocity) is introduced.

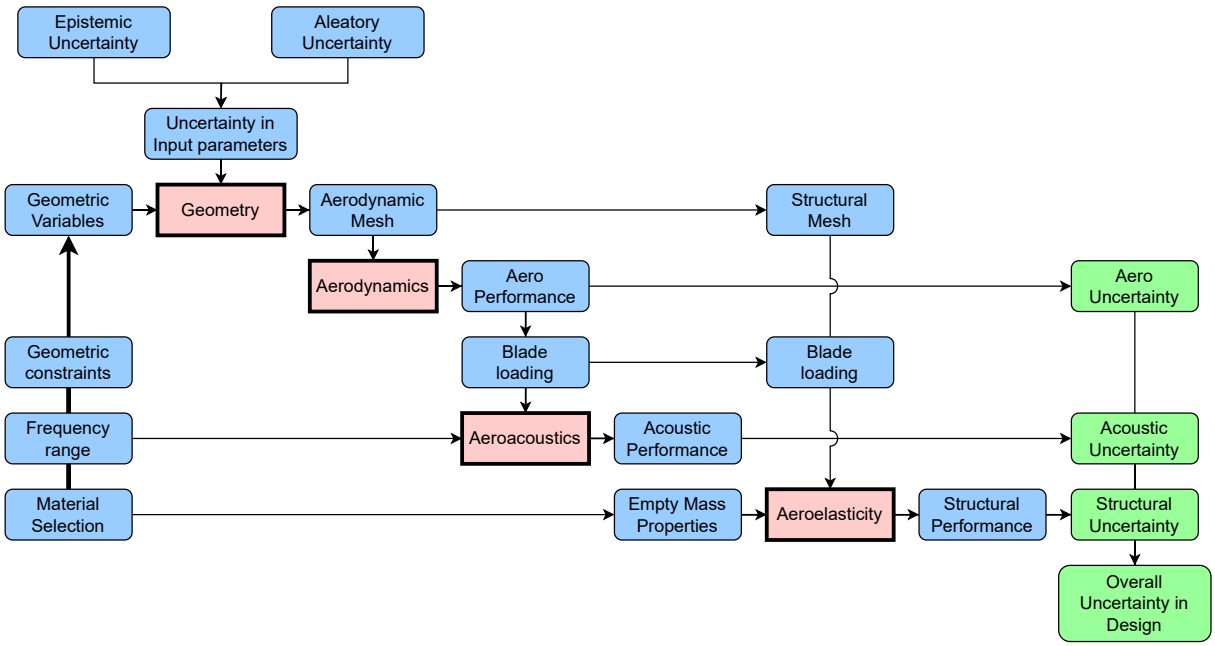


Fig. 5 Mixed Aleatory-Epistemic Uncertainty Propagation Framework

2) *Aleatory Uncertainty Quantification*: Following the initial stage, the framework employs traditional uncertainty quantification techniques (Monte Carlo Simulation) to address aleatory uncertainty with the sweep angle parameter.

After this quantification, another round of epistemic uncertainty value is prescribed using the second value of freestream velocity, for the interval analysis, to further refine the understanding of the system's behaviour under uncertain conditions.

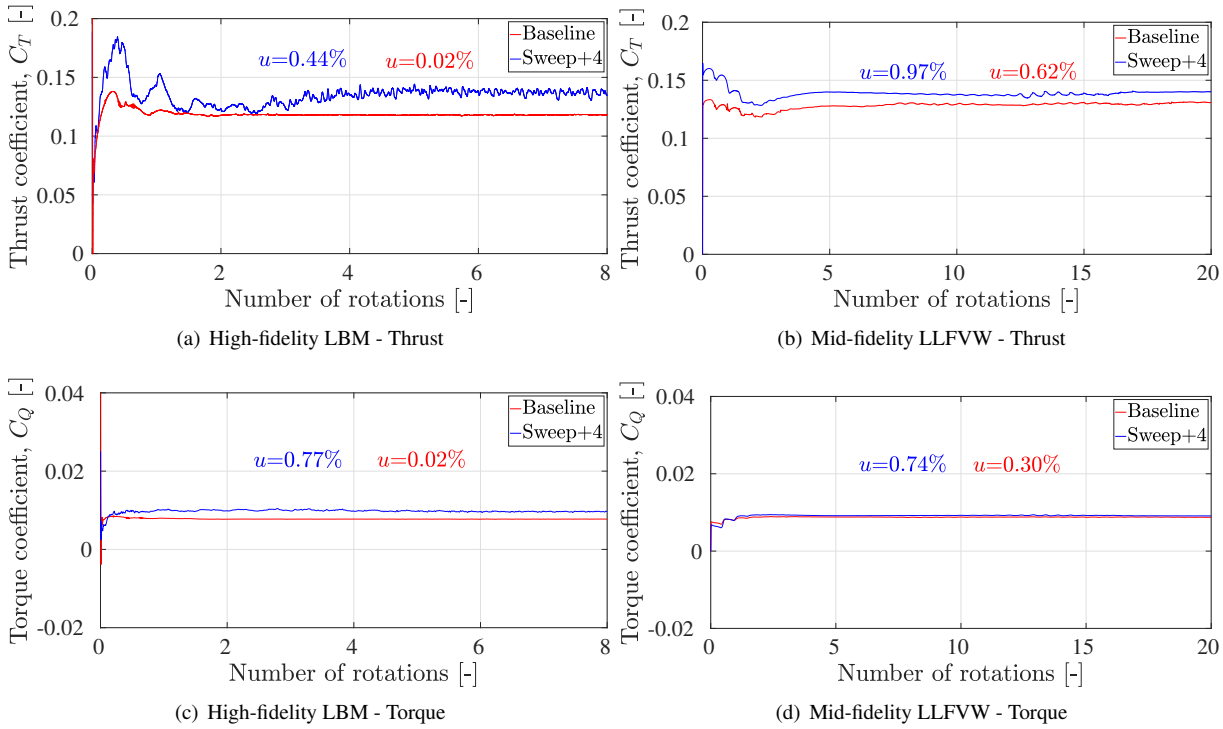
V. Results

A. Temporal convergence study and validation

Statistical temporal convergence characteristics of the thrust coefficient (C_T) and the torque coefficient (C_Q) for the baseline and sweep+4 configurations are shown in Figure 6. C_T is obtained by dividing thrust value with $\rho n^2 D^4$ and C_Q is obtained by dividing torque value with $\rho n^2 D^5$, where, ρ is density, n is rotations per second and D is propeller diameter. These results are obtained using both high-fidelity LBM and mid-fidelity LLFVW methods. The corresponding uncertainty values (u) are calculated as a percentage of the standard deviation of thrust and torque values after the 6th rotor rotation for high-fidelity and after the 10th rotor rotation for mid-fidelity. These uncertainty values reflect the degree of uncertainty or variability in the computed thrust and torque coefficients over time due to the inherent unsteadiness and randomness in the fluid dynamic interactions.

It is evident that the results obtained from the high-fidelity converge after at least 6 rotations, while the results from the mid-fidelity method converge after 17-18 rotations. The results for thrust show more unsteady variations than torque, which is observed for both the numerical methods employed. Furthermore, the sweep+4 configuration shows higher unsteady loading fluctuations than its baseline counterpart, especially for thrust values obtained using the high-fidelity method. This shows that there is a higher amount of fluid dynamic interactions between the blade and the flow in the former, which has a non-zero tip offset in the swept blade design, than in the latter. Finally, to ensure that statistical convergence is achieved for all parameters, all subsequent results in this study are derived from the 8th rotation for the high-fidelity and the 20th rotation for the mid-fidelity method.

Table 4 lists the high-fidelity and mid-fidelity results from the current study and the reference results by Casalino et al. [78]. The reference data consists of the experimental measurements for the propeller in a wind tunnel. A good agreement is observed between all of them, especially between high-fidelity and experimental results, for thrust



(a) High-fidelity LBM - Thrust

(b) Mid-fidelity LLFVW - Thrust

(c) High-fidelity LBM - Torque

(d) Mid-fidelity LLFVW - Torque

Fig. 6 Statistical temporal convergence study for thrust coefficient C_T and torque coefficient C_Q using high-fidelity LBM and mid-fidelity LLFVW

values (difference of 5.07%). Consequently, the current numerical setup is deemed sufficient to enable an accurate and insightful physical analysis of the fluid dynamic interactions and noise sources in a propeller.

Table 4 Average C_T and C_Q comparison using different methods and experimental validation for the baseline propeller

	High-fidelity LBM	**Mid-fidelity LLFVW**	**Experiment[78]**
Thrust coefficient, C_T[-]	0.118	0.1309	0.1123
Torque coefficient, C_Q[-]	0.0077	0.0088	0.0052

B. Interval analysis for epistemic uncertainty

In the context of multi-fidelity, multi-disciplinary uncertainty propagation, interval analysis serves as a powerful tool for managing uncertainties across various levels of fidelity and disciplinary interactions. By representing uncertain parameters and model outputs as intervals rather than fixed values, interval analysis allows for a comprehensive encapsulation of epistemic uncertainties inherent in complex aerodynamic, aeroacoustic, and structural models of propellers. This approach ensures that the propagated uncertainties through these interconnected models reflect the true range of possible outcomes, accommodating variations in model accuracy and data reliability, and leading to more robust and reliable engineering solutions in the field of aerospace design and analysis.

For the interval analysis, the freestream velocity range is between 0 and 10 m/s, which encapsulates most of the wind velocities in the urban environment which an air vehicle can encounter during its operation [18, 82, 83]. Table 5 lists the data for thrust and torque values and overall sound pressure level (OSPL) for the two freestream velocities obtained using high-fidelity LBM. For thrust and torque, both dimensional and non-dimensional values are reported for a better physical understanding of the phenomenon involved.

At 0 m/s, C_T is noted to be 0.118, which reflects the static thrust coefficient. At 10 m/s, C_T decreases to 0.067,

Table 5 Thrust and torque values (both dimensional and non-dimensional) and OSPL for different freestream velocities using high-fidelity LBM

Freestream velocity (m/s)	C_T (Thrust[N])	C_Q (Torque[Nm])	OSPL [dB]
0	0.118 (8.13 N)	0.0077 (0.159 Nm)	85.3
10	0.067 (4.65 N)	0.0066 (0.136 Nm)	50.15
Δ (Variation)	42.85%	14.29%	41.21%

indicating a 42.85% decrease. This reduction in thrust as the velocity increases is indicative of the reduced performance of the propeller at higher inflow speeds, due to a decrease in the angle of attack of the propeller blade. On the other hand, at 0 m/s, C_Q is 0.0077, representative of the static torque required to maintain the rotational speed of 5000 RPM. At 10 m/s, C_Q slightly decreases to 0.0066, showing only a 14.29% reduction. The less pronounced reduction in torque coefficient compared to thrust suggests less sensitivity of the propeller drag and skin friction values as compared to propeller lift values, to the increase in free stream velocity. For OSPL values, at 0 m/s, the noise generated is 85.3 dB, which is likely dominated by the tonal noise generation mechanisms and blade-vortex interactions at static/hover conditions [78]. At 10 m/s, the OSPL decreases to 50.15 dB, showing a 41.21% reduction. The reduction in noise level at higher velocities is attributed to a decrease in the dominant tonal noise generation mechanisms which is directly dependent on the thrust values of the propeller [84].

Table 6 lists the values for thrust, torque and absolute structural deflection at 50% r/R blade location, obtained using mid-fidelity LLFVW and the difference with the values obtained using the high-fidelity method. The Δ (variation) indicates the sensitivity of these parameters to changes in free stream velocity, while the differences between mid-fidelity and high-fidelity results (ΔC_T (high-fidelity) & ΔC_Q (high-fidelity)) indicate the inherent uncertainties in the whole framework due to differences in the aerodynamic methods employed (LBM and LLFVW). The latter is present only for aerodynamics, namely thrust and torque results.

Table 6 Thrust and torque values (both dimensional and non-dimensional) and structural deflection for different freestream velocities using mid-fidelity LLFVW

Freestream velocity (m/s)	C_T (Thrust[N])	ΔC_T (high-fidelity)	C_Q (Torque[Nm])	ΔC_Q (high-fidelity)	Absolute deflection at 50% r/R (m)
0	0.1309 (9.02 N)	10.95%	0.0088 (0.181 Nm)	13.83%	0.015
10	0.088 (6.06 N)	30.32%	0.0077 (0.158 Nm)	16.18%	0.010
Δ (Variation)	32.79%	-	12.44%	-	31.19%

Therefore, the analysis is bifurcated into two folds: (1) Interval analysis for input uncertainty due to varying free stream velocity, and (2) Uncertainty due to different fidelities used for aerodynamics.

For an increase of velocity from 0 m/s to 10 m/s, a significant decrease of 32.79% for C_T and 12.44% for C_Q is observed. For the absolute structural deflection at 50% of the blade radius (r/R), it decreases from 0.015 m at 0 m/s to 0.010 m at 10 m/s, a decrease of 31.19%. Overall, the interval analysis reveals the sensitivity of each parameter to changes in free stream velocity. Notably, C_T exhibits the highest sensitivity, observed both for mid and high-fidelity methods. It is closely followed by OSPL (using the high-fidelity method) and absolute deflection (using the mid-fidelity method) suggesting a direct relationship between these two parameters and the propeller thrust. Finally, the least sensitivity to changes in freestream velocity is shown by C_Q, observed both for mid and high-fidelity methods.

When comparing results for the two methods employed, the high-fidelity method shows a difference of 10.95% to 30.32% for C_T at 0 m/s and 10 m/s, respectively, compared to the mid-fidelity results. For C_Q, a discrepancy of 13.83% to 16.18% is noted. Overall, this shows that the uncertainty propagation framework incorporates uncertainty in the range of 13.83% to 30.32% due to different aerodynamic modelling methods employed, which is in addition to the uncertainty that may arise due to variation in operational parameters such as freestream velocity. This is called second-order uncertainty and needs to be taken into consideration when propagating uncertainty using mid or low-fidelity methods.

C. Aleatory uncertainty and effect of blade sweep

Figure 7 compares the average thrust coefficient C_T and torque coefficient (C_Q) for all the swept blade configurations considered in this study. The configurations include a baseline geometry and pairs of forward-swept (-2, -4) and backward-swept (+2, +4) blade configurations, the details of which are mentioned in Table 1. These results are reported from high-fidelity LBM simulations.

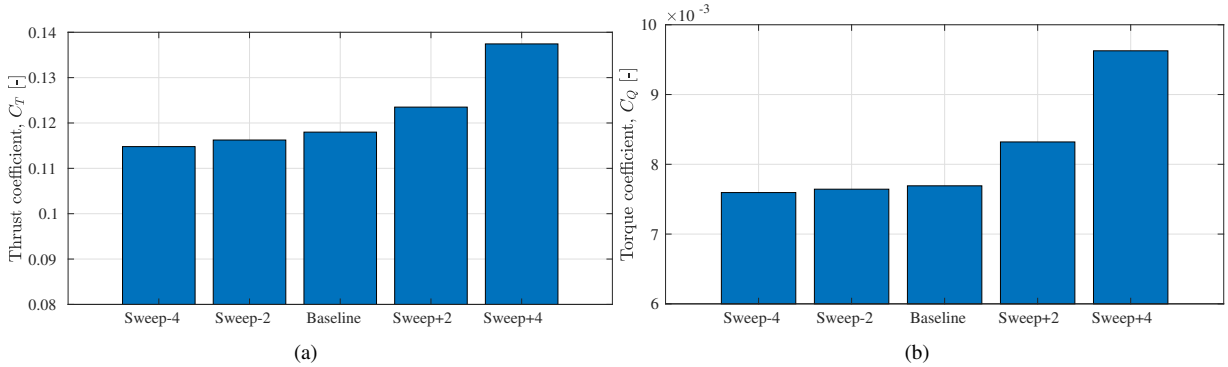


Fig. 7 Thrust coefficient C_T and torque coefficient C_Q comparison for different propeller blade sweep and the baseline propeller, using high-fidelity LBM

It is evident that increasing the backward sweep (indicated by +4 and +2) results in higher C_T values than the baseline geometry. Conversely, a forward sweep (indicated by -4 and -2) decreases thrust when compared to the baseline geometry. A marked increase is observed in C_Q for the +4 swept blade configuration, denoting that more torque is required for rotation, potentially due to an increase in drag forces for the backward swept blade design. The -4 configuration, however, presents a lower C_Q relative to the baseline, implying a reduction in the overall drag of the forward swept propeller.

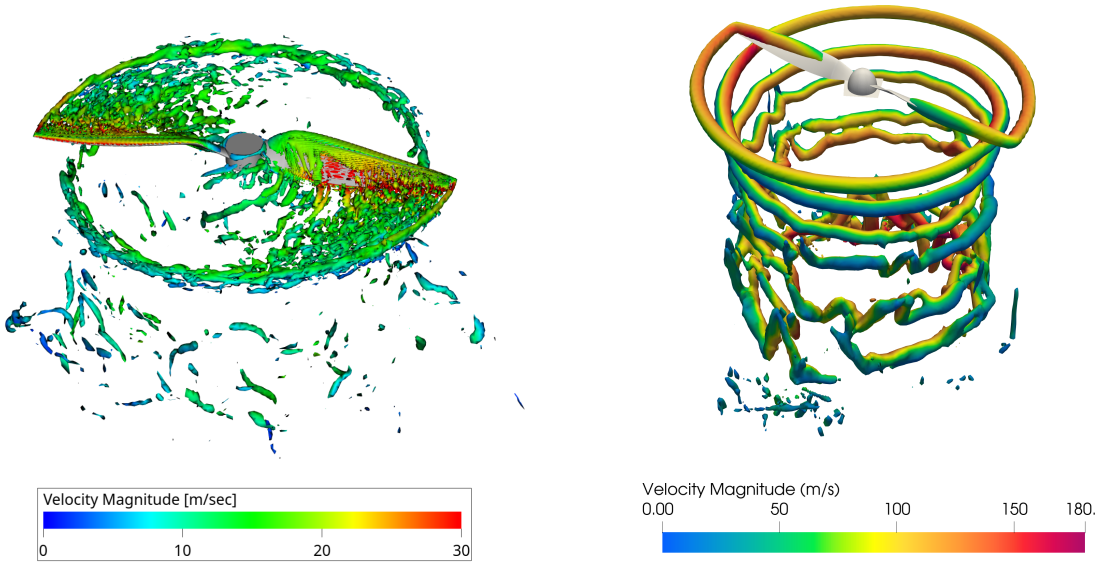
The patterns observed suggest that the sweep of the blade has a substantial influence on the aerodynamic performance of the propeller. A backward sweep appears to augment the thrust generation capability at the expense of higher torque demand. In contrast, a forward sweep reduces both thrust and torque, which may be beneficial in applications where efficiency is prioritized over maximum thrust output. The performance variations can be attributed to changes in the aerodynamic loading on the blades due to the sweep design. A backward sweep may lead to a favourable pressure gradient along the blade span, enhancing lift and delaying stall. Forward sweep, conversely, may result in a less favourable pressure distribution, reducing lift and thrust.

Figure 8 shows instantaneous 3D flowfield using iso-surfaces of the λ_2 criterion for vortices visualization, using high-fidelity and mid-fidelity methods. The tip vortices originating from the blade tips of the propeller exhibit a coherent flow pattern characterized by the formation of spiral vortex rings that encircle the axis of the turbine. As these large vortex structures move downstream, they undergo convective motion, resulting in wake contraction and fragmentation into smaller-scale structures due to flow instabilities and spatial modulation. Ultimately, these smaller vortex structures dissipate and mix with the surrounding fluid [85, 86]. These vortices lead to stronger blade vortex interaction (BVI), disrupting the ideal pressure and loading distribution along both the chordwise and spanwise directions of the propeller.

The figure also shows that the mid-fidelity method is unable to resolve small-scale structures in the 3D flowfield, as accurately as the high-fidelity method. This will lead to differences in blade-vortex interaction (BVI) and is one of the reasons for the difference observed in Table 4.

Figure 9 (a) and (b) display the variation of thrust and torque values against the tip offset. The data includes findings from both the high-fidelity and mid-fidelity simulations. Additionally, a Multi-Fidelity Kriging (MFK) interpolation curve, referred to as the "Kriging curve," is fitted through the data points to model the relationship between the tip offset and the respective performance metric. The predictions are made at unsampled tip offsets which will be used in the next step in the framework for uncertainty propagation.

In both figures, it is evident that the high-fidelity method estimates lower values of thrust and torque than the mid-fidelity method. The agreement is better for positive tip offsets (backward sweep) than for negative tip offsets. The discrepancy between the two methods may be attributed to the varying degrees of assumptions inherent in the mid-fidelity models. These differences tend to become more pronounced at larger negative tip offsets, possibly due to



(a) High-fidelity LBM

(b) Mid-fidelity LLFVW

Fig. 8 Instantaneous 3D flowfield using iso-surfaces of the λ_2 criterion for vortices visualization for the baseline propeller

increased aerodynamic interactions that the mid-fidelity method does not capture very effectively.

It is important to note that XFOIL polar values (C_l and C_d vs angle of attack α) are utilized in the analytical formulation of mid-fidelity LLFVW method, which influence the blade angle of attack and induced velocity, and this has a significant impact on the thrust and torque values obtained. It is suggested to modify these polars accordingly by introducing empirical corrections in future investigations [21**?**].

Figure 9 (c) and (d) display the variation of overall sound pressure level (OSPL) and absolute structural deflection at 50% r/R against the tip offset. The figures also show predictions made using Ordinary Kriging at unsampled data points. The former is obtained using the high-fidelity method while the latter is obtained using the low-fidelity method. Both the parameters show a similar variation to the thrust values using their corresponding numerical method. While the noise generation monotonically increases as tip offsets vary from -0.4 to 0.4, the structural deflection exhibits the lowest value for the baseline configuration (tip offset = 0).

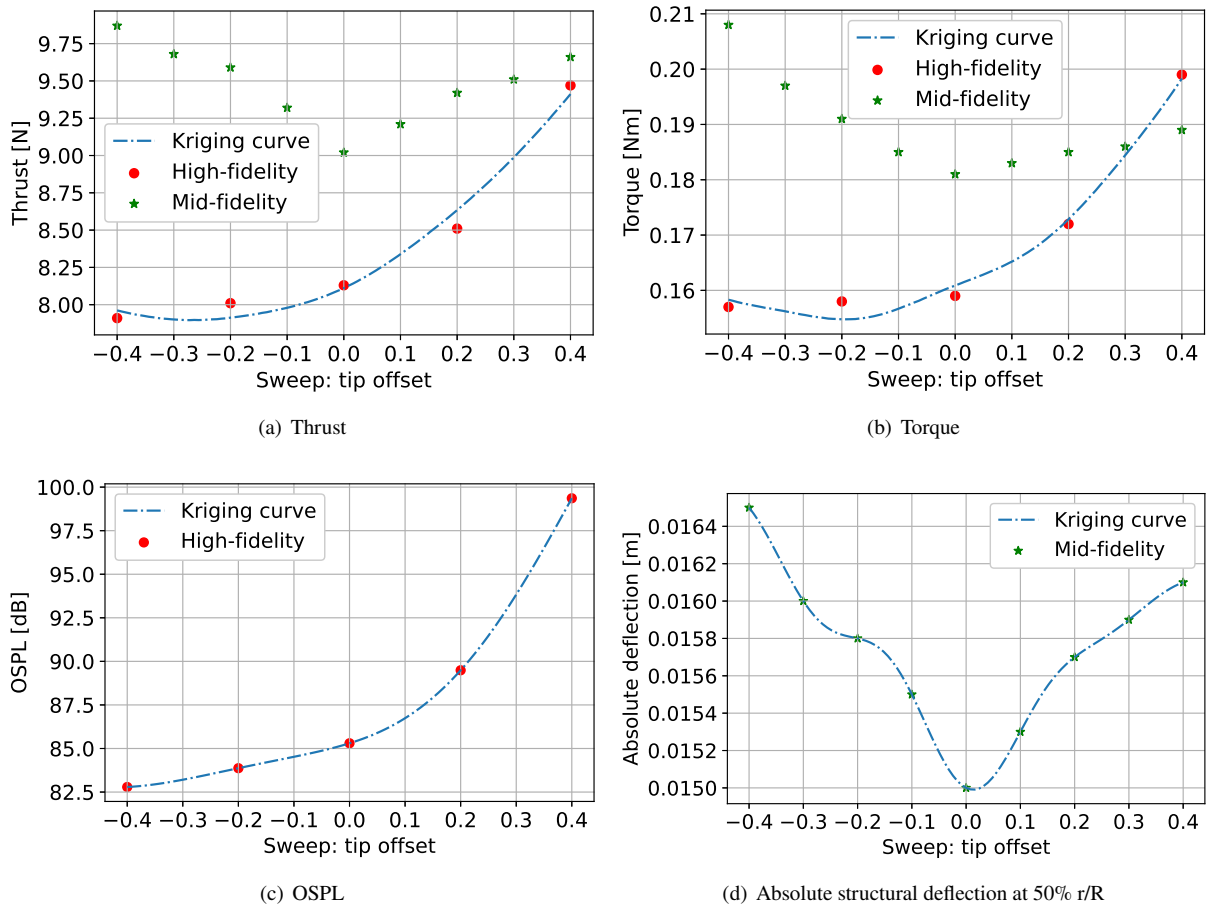
Table 7 presents the differential error obtained from the results of mid-fidelity and high-fidelity methods for various tip offsets. The data represents the uncertainty present in the framework due to the usage of multi-fidelity methods. The error is highest for the most forward sweep configuration (-0.4) and decreases monotonically towards the baseline and the most backward sweep configuration (+0.4).

Table 7 Differential error estimation for thrust and torque values predicted using the values obtained by mid-fidelity and high-fidelity methods

Tip offset	-0.4	-0.2	0	+0.2	+0.4
Uncertainty in thrust	24.78 %	19.73 %	10.95 %	10.69 %	2.00 %
Uncertainty in torque	32.48 %	20.89 %	13.84 %	7.56 %	5.03 %

Figure 10 represents histograms of sampled data superimposed with a probability density function (PDF) curve for the input parameter "tip offset." Each sub-figure corresponds to a different sampling technique: (a) Random, (b) Sobol, (c) Antithetic variates, and (d) Halton. For all curves, the PDF curve is generated for a normal (Gaussian) distribution with a mean at tip offset of 0 and a standard deviation of 0.15.

Figure 10 (a) depicts a random sampling distribution where the tip offset values are randomly selected from the input space. The PDF curve appears to fit well over the histogram, suggesting that the random samples approximate the



(a) Thrust

(b) Torque

(c) OSPL

(d) Absolute structural deflection at 50% r/R

Fig. 9 Values obtained using both the mid and high-fidelity methods for different blade sweep defined by tip offsets and curve predicted using Kriging

underlying distribution reasonably well. Figure 10 (b) shows the distribution of samples using the Sobol sequence, a quasi-random low-discrepancy sequence designed to cover the input space more uniformly than simple random sampling. It is particularly effective in higher dimensions where the curse of dimensionality makes random sampling less efficient. Figure 10 (c) illustrates the use of antithetic variates, a variance reduction technique where samples are chosen to be negatively correlated between pairs of samples to reduce the variance of the estimation. Finally, figure 10 (d) displays the Halton sequence sampling, another low-discrepancy, quasi-random method that, like the Sobol sequence, seeks to cover the input space more uniformly but uses a different method for generating the sequence.

In the context of uncertainty quantification and propagation, choosing the appropriate sampling method is crucial. While random sampling is easy to implement and does not depend on the dimensionality of the problem, quasi-random sequences like Sobol and Halton can offer more efficient coverage with fewer samples, leading to faster convergence in the estimation of uncertainty. Figure 11 presents scatter plots where the x-axis represents the tip offset, and the y-axis represents the thrust values predicted by the MFK method for the model solver in the framework. The spread and distribution of the data points vary according to the sampling method used, which affects the density and coverage of the input space.

For random sampling, the data points appear to be distributed haphazardly across the input space without consideration for evenness or stratification. For the Sobol sampling, a quasi-random, low-discrepancy sequence covers the input space more uniformly, which is reflected in the thrust data that appears to capture the trend with fewer irregularities or gaps in the data. With antithetic variates, the sampling leads to a more symmetric spread of data around the input space's median value, which may result in a more stable and reliable prediction curve, particularly for estimating the expected value of the output. Finally, the Halton sequence provides a different pattern of spread in the input space and the thrust

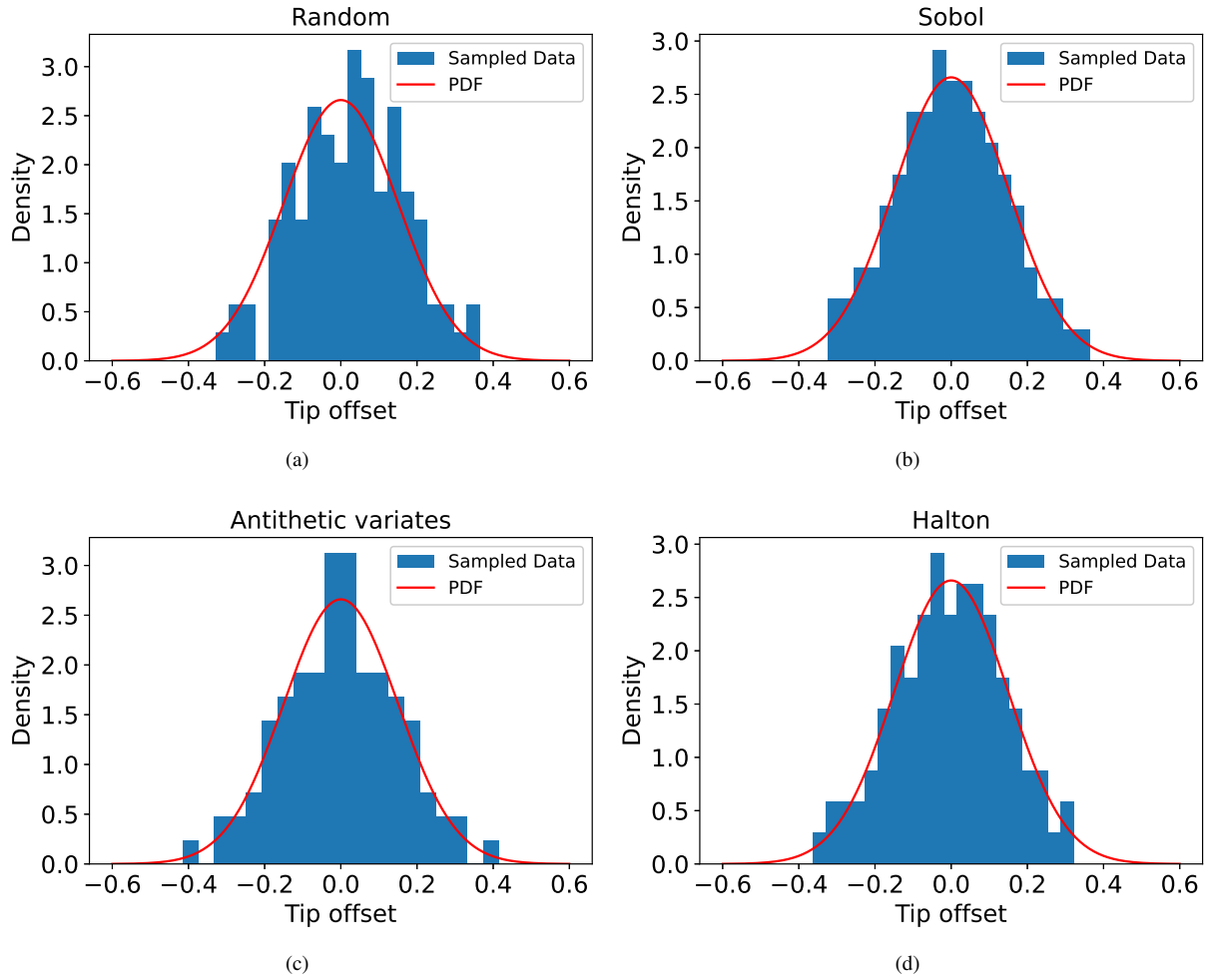


Fig. 10 Different sampling methods used in this study along with probability density function of the tip offset parameter for uncertainty quantification

values align well with the trend predicted by the sequence, demonstrating the method's effectiveness in covering the input space efficiently.

Figure 12 presents graphically the convergence behaviour of statistical metrics for thrust values obtained via the four distinct sampling methods discussed previously. The analysis is critical in understanding the reliability and accuracy of these methods for uncertainty quantification and propagation in a complex model. Each sub-figure plots these metrics against the number of samples, ranging from 0 to 10,000. The convergence of the mean indicates the stability of the sampling methods over the number of samples, while the error in mean reflects the absolute difference between the sampled mean and the true or analytical mean. In this study, the true mean is calculated from random sampling for 100,000 samples, although the high-fidelity value can also be assumed as the true mean.

Notably, the Sobol and Halton sequences demonstrate a more stable convergence of mean to a specific value, reflecting the robustness of low-discrepancy, quasi-random sequences in exploring the input space efficiently. The random and antithetic methods show greater fluctuations initially, which stabilize as the number of samples increases, suggesting higher variability in their estimates. The Sobol and Halton sequences result in a lower error, and hence a higher accuracy, more quickly than random and antithetic sampling. This characteristic is particularly important in the context of high-dimensional problems, where accurate mean estimation is critical. The faster convergence of any method implies fewer required samples, which can significantly reduce computational costs.

Figure 12 (c) shows the variance convergence, which is indicative of the reliability of the sampling methods in capturing the spread of the data, while Figure 12 (d) shows the error in variance which indicates how quickly the

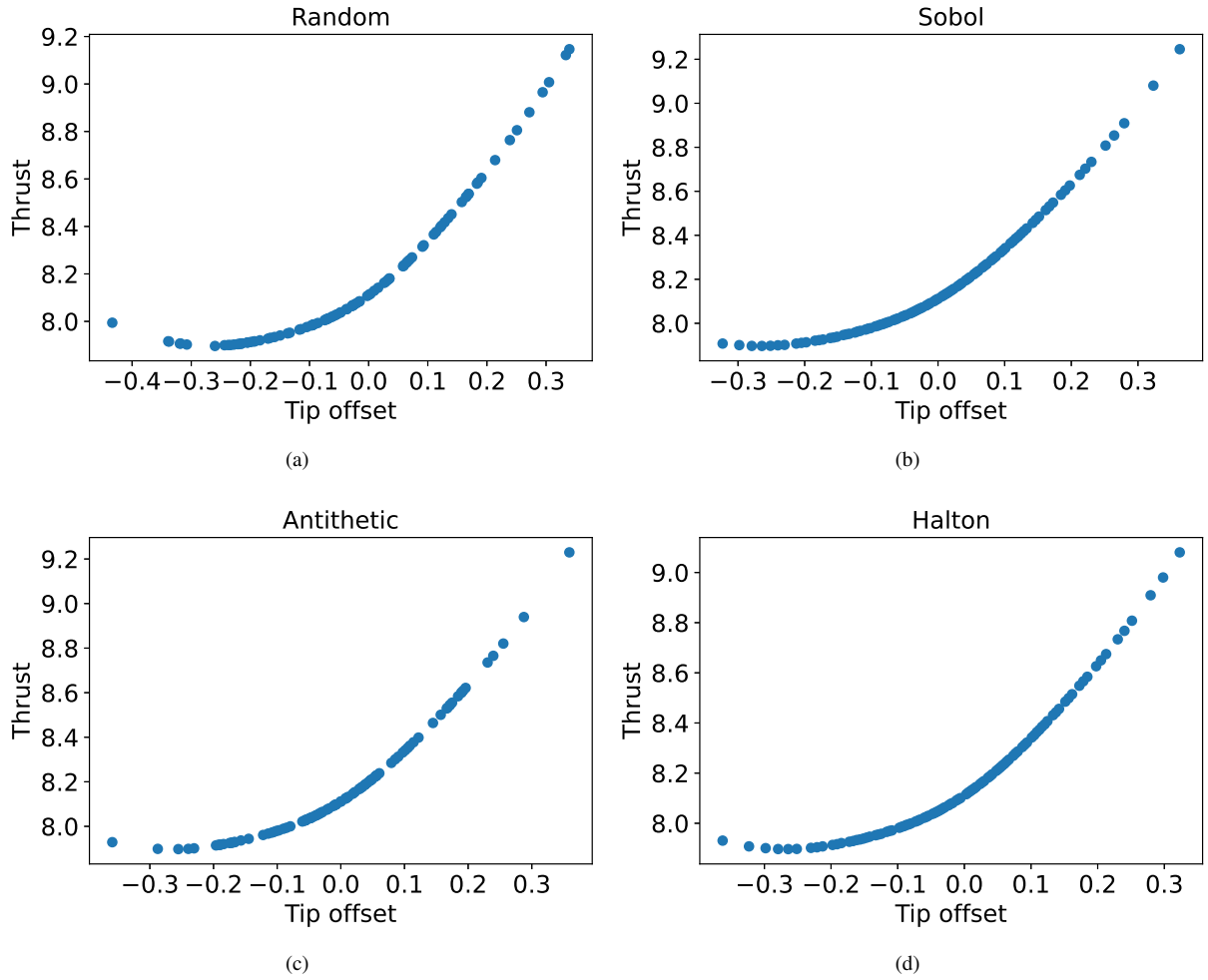


Fig. 11 Scatter plot for thrust values as predicted by the MFK method using various sampling methods, for 100 samples (as an example); mean is at tip offset = 0 with a standard deviation of 0.15; Thrust values are in N

estimated variance of the sampling methods approaches the true variance. Again, the quasi-random Sobol and Halton sequences tend to have a smoother and quicker convergence, both for variance and error in variance, depicting their efficiency in reflecting the true variability of the model output. This behaviour ensures a more systematic and uniform exploration of the input space, leading to more accurate and reliable statistical estimates. Even though Sobol and Halton are similar in behaviour, the latter is chosen for further uncertainty quantification and analysis due to its smoother and faster convergence characteristics amongst the two sequences.

Table 8 presents a systematic analysis of uncertainty propagation for the propeller, focusing on the impact of varying the tip offset. The study investigates the effect of this parameter on four output variables: Thrust, Torque, Overall Sound Pressure Level (OSPL), and Structural Deflection at 50% r/R. The case 1 baseline scenario with no sweep (mean tip offset = 0) shows relatively low variability in thrust, OSPL and structural deflection as compared to torque, with the least variability being shown by the structural deflection. Notably, the data for structural deflection also contains the uncertainty which arises due to the usage of only the mid-fidelity method.

For case 2 (mean tip offset = 0.2) with a backward sweep, an increase in both the mean and variability of all parameters is observed, indicating an increase in the sensitivity of these outputs to the sweep design changes, suggesting that as the propeller blades are swept backwards, the system becomes more responsive but also less predictable. Again, torque has the highest uncertainty and structural deflection has the least. This increased uncertainty for backward sweep can also be understood from the plots presented in Figure 9, where the slope of plots is higher for backward sweep values as compared to the baseline. For case 3 (mean tip offset = -0.2) with a forward sweep, there's a decrease in the

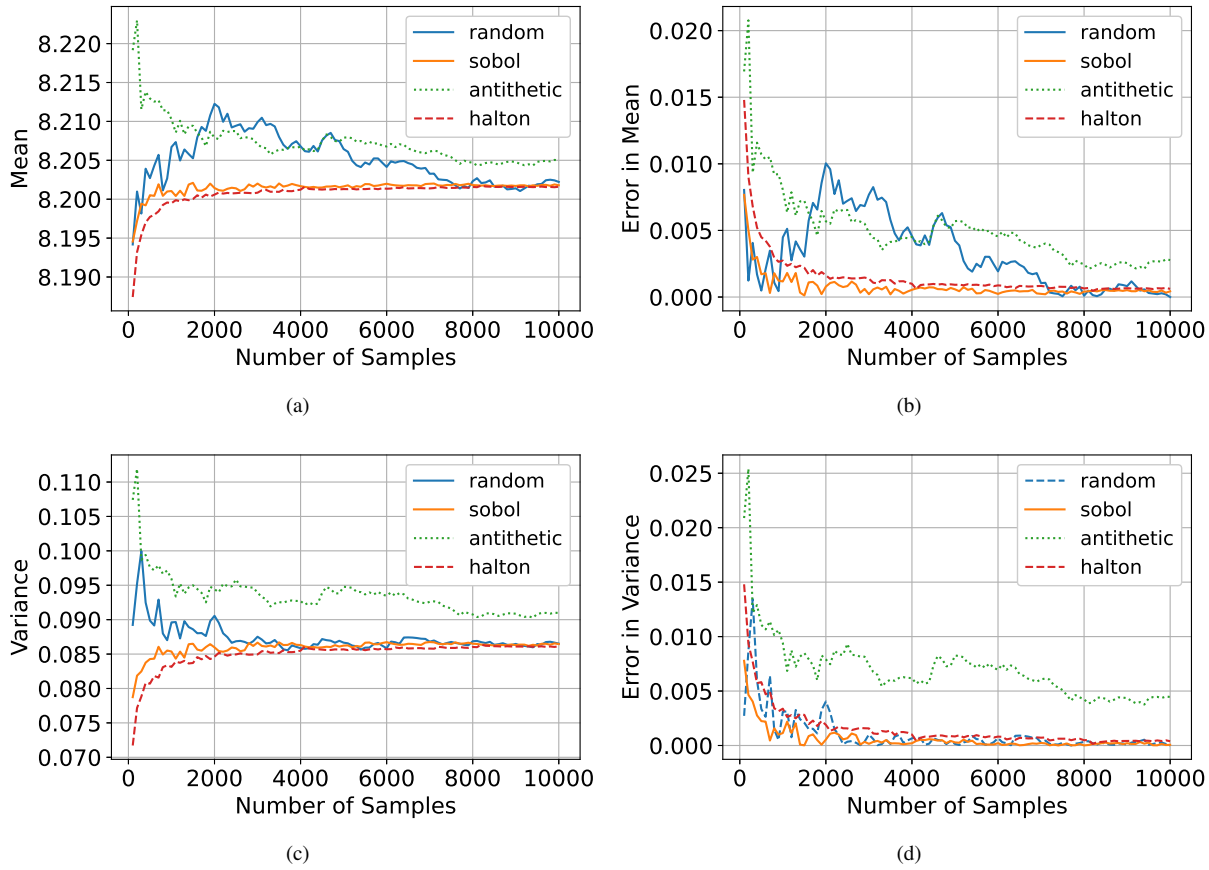


Fig. 12 Convergence behaviour of statistical metrics for thrust values obtained using four different sampling methods; y-axis of all sub-figures are in N

Table 8 Uncertainty propagation for four different parameters of interest using the Halton sequence

		Sweep (tip offset)	Thrust [N]	Torque [Nm]	OSPL [dB]	Structural deflection [m]
1	**Mean**	0	8.201	0.163	86.08	0.0154
	Standard deviation	0.15	0.293 (3.57%)	7.691e-3 (4.72%)	2.612 (3.03%)	3.312e-4 (2.15%)
2	**Mean**	0.2	8.706	0.177	90.95	0.0156
	Standard deviation	0.15	0.493 (5.66 %)	1.489e-2 (8.41 %)	5.423 (5.96 %)	3.419e-4 (2.19 %)
3	**Mean**	-0.2	7.983	0.158	84.03	0.0158
	Standard deviation	0.15	0.121 (1.52 %)	4.162e-3 (2.63 %)	1.084 (1.29 %)	4.229e-4 (2.68 %)

mean and variability of thrust, torque and OSPL, while there is a corresponding increase for structural deflection. This suggests that forward sweep contributes to a more consistent and better aerodynamic and aeroacoustic performance and the system's behaviour is comparatively stable and predictable. However, the mean thrust value is reduced and there is an increased uncertainty in structural performance.

VI. Conclusions and Discussions

The present research performs an in-depth investigation into the uncertainty quantification and propagation of mixed uncertainties in a multi-fidelity multi-disciplinary framework. Three different disciplines are investigated -

aerodynamics, aeroacoustics and aeroelasticity. For a test case, propeller blade design with sweep is studied with blade tip offset and freestream velocity as the uncertain parameters. The Lattice Boltzmann Method (LBM) is employed as the high-fidelity method, complemented by aeroacoustic post-processing via the Ffowcs-Williams and Hawkings (FW-H) approach for far-field noise estimation. Additionally, mid-fidelity simulations are performed utilizing the Lifting Line Free Vortex Wake (LLFVW) and Finite Element Analyses (FEA) methods. A 2-bladed propeller with 0.3m diameter is utilized and nine distinct sweep configurations are analyzed, including the baseline configuration with no sweep.

The statistical temporal convergence of the baseline configuration is achieved just after 2-3 rotor rotations while for the backward swept configuration, it takes 6 rotor rotations, using high-fidelity LBM and with lower uncertainty in unsteady blade loading for the former. Similarly, the mid-fidelity method shows faster convergence for the former than the latter. Also, torque values exhibit faster convergence (in 2 rotations) than thrust values (in 6 rotations) using high-fidelity LBM. For epistemic uncertainty, freestream velocity is taken as the uncertain parameter for interval analysis. For an increase of velocity from 0 to 10 m/s, thrust shows the maximum variability (42.85%), closely followed by OSPL (41.21%) and absolute structural deflection at 50% r/R (31.19%), and torque shows the least variability (12.44 - 14.29 %). This is shown by both the mid and high-fidelity methods. Furthermore, differential analysis reveals an uncertainty in the range of 13.83% to 30.32% due to the usage of a multi-fidelity approach.

For aleatory uncertainty, the blade tip offset, which characterizes blade sweep, is taken as the uncertain parameter. Both the numerical methods show an increase in thrust and torque when the blade is swept backwards with the difference between the prediction made by the two methods decreasing with higher sweep (at the largest sweep, a difference of 2% in thrust and 5.03% in torque). On the contrary, the high-fidelity method shows a decreasing trend and the low-fidelity method shows an increasing trend as the blade is swept forward. The highest uncertainty between the two methods is for the most forward swept (24.78 - 32.48 %) and the lowest uncertainty is for the most backward swept (2 - 5.03 %).

Four different sampling methods are used: Random, Sobol, Antithetic variates and Halton. The quasi-random Sobol and Halton sequences cover the input space more uniformly and capture the trend in thrust data with fewer irregularities or gaps, as compared to Random and Antithetic variates. The former also exhibits a more stable convergence and fewer fluctuations of various statistical metrics - Mean, Error in Mean, Variance and Error in Variance, as compared to the latter.

The uncertainty in the sweep parameter is propagated differently across various performance metrics of the propeller. The backward sweep increases the mean (by 5-6 %) and uncertainty (by 2-4 %) in all parameters, including thrust, torque, OSPL and structural deflection, indicating a potential increase in performance but with higher uncertainty. Conversely, the forward sweep is associated with reduced mean thrust and torque performance (by 2-3 %) and a reduction in uncertainty (by 4-6 %), implying a more reliable but possibly less efficient propeller operation. These insights will allow for an informed trade-off between performance enhancement and risk mitigation. The Halton sequence, as used in the analysis, has proven effective in capturing the nuances of uncertainty propagation across these diverse output variables.

Building on the findings of this research, future studies could explore extending the current methodology to a wider range of operating conditions and aircraft design problems, which would validate and potentially enhance the robustness of the proposed approach. Using other methods such as Non-Intrusive Polynomial Chaos (NIPC), Pseudo-spectral projection and Intrusive Galerkin could offer more efficient and accurate predictions of uncertainty propagation and quantification. Furthermore, integrating multi-objective optimization into the current framework could yield insights into optimizing the aircraft design process more effectively with increased robustness and reliability. Lastly, considering the environmental and economic aspects of propeller and aircraft component design in future studies could align the technical advancements with sustainable development goals, offering a holistic approach to aircraft design optimization.

Acknowledgments

This project has received funding from Innovate UK under Grant Agreement No 10003388. Nottingham Trent University has received sponsorship from 3DS Simulia for the commercial software PowerFLOW.

References

[1] Adkins, K. A., "Urban flow and small unmanned aerial system operations in the built environment," *International Journal of Aviation, Aeronautics, and Aerospace*, Vol. 6, No. 1, 2019, p. 10.

[2] Deters, R. W., *Performance and slipstream characteristics of small-scale propellers at low Reynolds numbers*, University of Illinois at Urbana-Champaign, 2014.

[3] Nagy, A. B., Delfs, J., and Bennett, G. J., "Aeroacoustics research in Europe: The CEAS-ASC report on 2020 & 2021 highlights," *Journal of Sound and Vibration*, Vol. 534, 2022, p. 117002.

[4] Atassi, H. M., *Unsteady aerodynamics, aeroacoustics, and aeroelasticity of turbomachines and propellers*, Springer Science & Business Media, 2012.

[5] CHANG, L., and SULLIVAN, J., "Optimization of propeller blade shape by an analytical method," *18th Joint Propulsion Conference*, 1982, p. 1125.

[6] Cho, J., and Lee, S.-C., "Propeller blade shape optimization for efficiency improvement," *Computers & fluids*, Vol. 27, No. 3, 1998, pp. 407–419.

[7] Xia, X., Ma, D., Zhang, L., Liu, X., and Cong, K., "Blade shape optimization and analysis of a propeller for VTOL based on an inverse method," *Applied Sciences*, Vol. 12, No. 7, 2022, p. 3694.

[8] Toman, U. T., Hassan, A.-K. S., Owis, F. M., and Mohamed, A. S., "Blade shape optimization of an aircraft propeller using space mapping surrogates," *Advances in Mechanical Engineering*, Vol. 11, No. 7, 2019, p. 1687814019865071.

[9] Wu, Y., Ai, Y.-t., Ze, W., Jing, T., Song, X., and Chen, Y., "A novel aerodynamic noise reduction method based on improving spanwise blade shape for electric propeller aircraft," *International Journal of Aerospace Engineering*, Vol. 2019, 2019, pp. 1–10.

[10] Sullivan, J., "The effect of blade sweep on propeller performance," *10th Fluid and Plasmadynamics Conference*, 1977, p. 716.

[11] Bergmann, O., Möhren, F., Braun, C., and Janser, F., "Aerodynamic Analysis of Swept Propeller with BET and RANS," *DLRK 2021*, 2021.

[12] Rohrbach, C., "A report on the aerodynamic design and wind tunnel test of a prop-fan model," *12th Propulsion Conference*, 1976, p. 667.

[13] Delano, J. B., and Harrison, D. E., "Investigation of the NACA 4-(4)(06)-057-45A and NACA 4-(4)(06)-057-45B Two-blade Swept Propellers at Forward Mach Numbers to 0.925," Tech. rep., 1950.

[14] Evans, A. J., and Liner, G., "A wind-tunnel investigation of the aerodynamic characteristics of a full-scale sweptback propeller and two related straight propellers," Tech. rep., 1951.

[15] West, T. K., and Gumbert, C., "Multifidelity, multidisciplinary uncertainty quantification with non-intrusive polynomial chaos," *58th AIAA/ASCE/AHS/ASC Structures, Structural Dynamics, and Materials Conference*, 2017, p. 1936.

[16] Chaudhuri, A., Lam, R., and Willcox, K., "Multifidelity uncertainty propagation via adaptive surrogates in coupled multidisciplinary systems," *AIAA journal*, Vol. 56, No. 1, 2018, pp. 235–249.

[17] Kipouros, T., Pachidis, V., Ghisu, T., and Templalexis, I., "Characterisation of the uncertainties of the operating conditions in turbomachinery design," *Turbo Expo: Power for Land, Sea, and Air*, Vol. 43987, 2010, pp. 793–802.

[18] Shubham, S., Wright, N., Avallone, F., and Ianakiev, A., "Aerodynamic and aeroacoustic investigation of vertical axis wind turbines with different number of blades using mid-fidelity and high-fidelity methods," *AIAA AVIATION 2023 Forum*, 2023, p. 3642.

[19] Ramprakash, T. T., Shubham, S., and Ianakiev, A., "Effect of Blade Shape on Aerodynamic and Aeroacoustic characteristics of Vertical Axis Wind Turbines using mid-fidelity and high-fidelity methods," *AIAA SciTech Forum*, 2024.

[20] Shubham, S., Avallone, F., Brandetti, L., Wright, N., and Ianakiev, A., "Effect of struts and central tower on aerodynamics and aeroacoustics of vertical axis wind turbines using mid-fidelity and high-fidelity methods," *AIAA SciTech Forum*, 2024.

[21] Marten, D., Bianchini, A., Pechlivanoglou, G., Balduzzi, F., Nayeri, C. N., Ferrara, G., Paschereit, C. O., and Ferrari, L., "Effects of airfoil's polar data in the stall region on the estimation of Darrieus wind turbine performance," *Journal of Engineering for Gas Turbines and Power*, Vol. 139, No. 2, 2017.

[22] Balduzzi, F., Marten, D., Bianchini, A., Drofelnik, J., Ferrari, L., Campobasso, M. S., Pechlivanoglou, G., Nayeri, C. N., Ferrara, G., and Paschereit, C. O., "Three-dimensional aerodynamic analysis of a Darrieus wind turbine blade using computational fluid dynamics and lifting line theory," *Journal of Engineering for Gas Turbines and Power*, Vol. 140, No. 2, 2018.

[23] Van Garrel, A., "Development of a wind turbine aerodynamics simulation module," 2003.

[24] Marten, D., "QBlade Guidelines v0. 95," *Technical University of Berlin, Berlin, Germany*, 2016.

[25] Marten, D., Lennie, M., Pechlivanoglou, G., Nayeri, C. N., and Paschereit, C. O., "Implementation, optimization, and validation of a nonlinear lifting line-free vortex wake module within the wind turbine simulation code qblade," *Journal of Engineering for Gas Turbines and Power*, Vol. 138, No. 7, 2016.

[26] Marten, D., Pechlivanoglou, G., Navid Nayeri, C., and Oliver Paschereit, C., "Nonlinear lifting line theory applied to vertical axis wind turbines: Development of a practical design tool," *Journal of Fluids Engineering*, Vol. 140, No. 2, 2018.

[27] Bergami, L., and Gaunaa, M., "ATEFlap Aerodynamic Model, a dynamic stall model including the effects of trailing edge flap deflection," 2012.

[28] Wendler, J., Marten, D., Pechlivanoglou, G., Nayeri, C. N., and Paschereit, C. O., "An unsteady aerodynamics model for lifting line free vortex wake simulations of hawt and vawt in qblade," *Turbo Expo: Power for Land, Sea, and Air*, Vol. 49873, American Society of Mechanical Engineers, 2016, p. V009T46A011.

[29] Gourdain, N., Jardin, T., Serre, R., Prothin, S., and Moschetta, J.-M., "Application of a lattice Boltzmann method to some challenges related to micro-air vehicles," *International Journal of Micro Air Vehicles*, Vol. 10, No. 3, 2018, pp. 285–299.

[30] Shubham, S., Avallone, F., Grande, E., and Casalino, D., "Computational Aeroacoustic Investigation of Co-rotating rotors for Urban Air Mobility," *Delft International Conference on Urban Air-Mobility*, 2021.

[31] Shubham, S., "Computational Aeroacoustic Investigation of Co-rotating rotors for Urban Air Mobility," 2020.

[32] Avallone, F., van den Ende, L., Li, Q., Ragni, D., Casalino, D., Eitelberg, G., and Veldhuis, L., "Aerodynamic and aeroacoustic effects of swirl recovery vanes length," *Journal of Aircraft*, Vol. 56, No. 6, 2019, pp. 2223–2235.

[33] Casalino, D., Hazir, A., and Mann, A., "Turbofan broadband noise prediction using the lattice Boltzmann method," *AIAA Journal*, Vol. 56, No. 2, 2018, pp. 609–628.

[34] Nardari, C., Casalino, D., Polidoro, F., Coralic, V., Lew, P.-T., and Brodie, J., "Numerical and experimental investigation of flow confinement effects on UAV rotor noise," *25th AIAA/CEAS Aeroacoustics Conference*, 2019, p. 2497.

[35] Succi, S., *The lattice Boltzmann equation for fluid dynamics and beyond*, 1st ed., Clarendon Press, Oxford, 2001.

[36] Shan, X., Yuan, X.-F., and Chen, H., "Kinetic theory representation of hydrodynamics: a way beyond the Navier–Stokes equation," *Journal of Fluid Mechanics*, Vol. 550, 2006, pp. 413–441. https://doi.org/10.1017/S0022112005008153, URL http://www.journals.cambridge.org/abstract_S0022112005008153.

[37] Chen, S., and Doolen, G., "Lattice Boltzmann method for fluid flows," *Annual Review of Fluid Mechanics*, Vol. 30, No. 1, 1998, pp. 329–364. https://doi.org/10.1146/annurev.fluid.30.1.329, URL http://www.annualreviews.org/doi/10.1146/annurev.fluid.30.1.329.

[38] Chen, H., Chen, S., and Matthaeus, W., "Recovery of the Navier-Stokes equations using a lattice-gas Boltzmann method," *Physical Review A*, Vol. 45, No. 8, 1992, pp. R5339–R5342. https://doi.org/10.1103/PhysRevA.45.R5339, URL https://link.aps.org/doi/10.1103/PhysRevA.45.R5339.

[39] Chen, H., Zhang, R., and Gopalakrishnan, P., "Lattice Boltzmann Collision Operators Enforcing Isotropy and Galilean Invariance," , 8 2015. URL https://patents.google.com/patent/US20150356217A1/en.

[40] Yakhot, V., and Orszag, S., "Renormalization group analysis of turbulence. I. Basic theory," *Journal of Scientific Computing*, Vol. 1, No. 1, 1986, pp. 3–51. https://doi.org/10.1007/BF01061452, URL http://link.springer.com/10.1007/BF01061452.

[41] Teixeira, C., "Incorporating Turbulence Models into the Lattice-Boltzmann Method," *International Journal of Modern Physics C*, Vol. 09, No. 08, 1998, pp. 1159–1175. https://doi.org/10.1142/S0129183198001060, URL http://www.worldscientific.com/doi/abs/10.1142/S0129183198001060.

[42] Wilcox, D., *Turbulence modelling for CFD (Third Edition)*, DCW Industries, Incorporated, 2006.

[43] Launder, B., and Spalding, D., "The numerical computation of turbulent flows," *Computer Methods in Applied Mechanics and Engineering*, Vol. 3, No. 2, 1974, pp. 269–289. https://doi.org/10.1016/0045-7825(74)90029-2, URL http://www.sciencedirect.com/science/article/pii/0045782574900292.

[44] Tasora, A., Serban, R., Mazhar, H., Pazouki, A., Melanz, D., Fleischmann, J., Taylor, M., Sugiyama, H., and Negrut, D., "Chrono: An open source multi-physics dynamics engine," *High Performance Computing in Science and Engineering: Second International Conference, HPCSE 2015, Soláň, Czech Republic, May 25-28, 2015, Revised Selected Papers 2*, Springer, 2016, pp. 19–49.

[45] Projectchrono.org, "Project Chrono - An Open-Source Physics Engine," *URL https://projectchrono.org/about/*, 2019.

[46] Tuxfamily, "EIGEN - a C++ template library for linear algebry : matrices, vectors, numerical solvers and related algorithms," *URL http://eigen.tuxfamily.org*, ????

[47] Recuero, A., and Negrut, D., "Co-rotational formulation in chrono," *ProjectCHRONO, Technical documentation, Università di Parma, Parma, Italy, accessed Feb*, Vol. 19, 2016, p. 2018.

[48] Marten, D., "QBlade: a modern tool for the aeroelastic simulation of wind turbines," 2020.

[49] Simeon, B., and Arnold, M., "Coupling DAEs and PDEs for simulating the interaction of pantograph and catenary," *Mathematical and Computer Modelling of Dynamical Systems*, Vol. 6, No. 2, 2000, pp. 129–144.

[50] Ffowcs Williams, J. E., and Hawkings, D. L., "Sound generation by turbulence and surfaces in arbitrary motion," *Philosophical Transactions of the Royal Society of London. Series A, Mathematical and Physical Sciences*, Vol. 264, No. 1151, 1969, pp. 321–342.

[51] Farassat, F., and Succi, G. P., "A review of propeller discrete frequency noise prediction technology with emphasis on two current methods for time domain calculations," *Journal of Sound and Vibration*, Vol. 71, No. 3, 1980, pp. 399–419.

[52] Brès, G., Pérot, F., and Freed, D., "Properties of the lattice Boltzmann method for acoustics," *15th AIAA/CEAS Aeroacoustics Conference (30th AIAA Aeroacoustics Conference)*, 2009, p. 3395.

[53] Casalino, D., "An advanced time approach for acoustic analogy predictions," *Journal of Sound and Vibration*, Vol. 261, No. 4, 2003, pp. 583–612.

[54] Toal, D. J., "Applications of multi-fidelity multi-output Kriging to engineering design optimization," *Structural and Multidisciplinary Optimization*, Vol. 66, No. 6, 2023, p. 125.

[55] Forrester, A. I., Keane, A. J., and Bressloff, N. W., "Design and analysis of" Noisy" computer experiments," *AIAA journal*, Vol. 44, No. 10, 2006, pp. 2331–2339.

[56] Jones, D. R., Schonlau, M., and Welch, W. J., "Efficient global optimization of expensive black-box functions," *Journal of Global optimization*, Vol. 13, 1998, pp. 455–492.

[57] Toal, D. J., and Keane, A. J., "Efficient multipoint aerodynamic design optimization via cokriging," *Journal of Aircraft*, Vol. 48, No. 5, 2011, pp. 1685–1695.

[58] Giles, M. B., "Collected matrix derivative results for forward and reverse mode algorithmic differentiation," *Advances in Automatic Differentiation*, Springer, 2008, pp. 35–44.

[59] Toal, D. J., Bressloff, N., Keane, A., and Holden, C., "The development of a hybridized particle swarm for kriging hyperparameter tuning," *Engineering optimization*, Vol. 43, No. 6, 2011, pp. 675–699.

[60] Eberhart, R., and Kennedy, J., "A new optimizer using particle swarm theory," *MHS'95. Proceedings of the sixth international symposium on micro machine and human science*, Ieee, 1995, pp. 39–43.

[61] Kennedy, M. C., and O'Hagan, A., "Predicting the output from a complex computer code when fast approximations are available," *Biometrika*, Vol. 87, No. 1, 2000, pp. 1–13.

[62] Metropolis, N., and Ulam, S., "The monte carlo method," *Journal of the American statistical association*, Vol. 44, No. 247, 1949, pp. 335–341.

[63] Helton, J. C., Johnson, J. D., Sallaberry, C. J., and Storlie, C. B., "Survey of sampling-based methods for uncertainty and sensitivity analysis," *Reliability Engineering & System Safety*, Vol. 91, No. 10-11, 2006, pp. 1175–1209.

[64] Landau, D., and Binder, K., *A guide to Monte Carlo simulations in statistical physics*, Cambridge university press, 2021.

[65] Xiu, D., and Karniadakis, G. E., "The Wiener–Askey polynomial chaos for stochastic differential equations," *SIAM journal on scientific computing*, Vol. 24, No. 2, 2002, pp. 619–644.

[66] Liu, J. S., and Liu, J. S., *Monte Carlo strategies in scientific computing*, Vol. 75, Springer, 2001.

[67] Shonkwiler, R. W., and Mendivil, F., *Explorations in monte carlo methods*, Springer Science & Business Media, 2009.

[68] Robert, C. P., Casella, G., and Casella, G., *Monte Carlo statistical methods*, Vol. 2, Springer, 1999.

[69] Cunha Jr, A., Nasser, R., Sampaio, R., Lopes, H., and Breitman, K., "Uncertainty quantification through the Monte Carlo method in a cloud computing setting," *Computer Physics Communications*, Vol. 185, No. 5, 2014, pp. 1355–1363.

[70] Hu, X., Chen, X., Parks, G. T., and Yao, W., "Review of improved Monte Carlo methods in uncertainty-based design optimization for aerospace vehicles," *Progress in Aerospace Sciences*, Vol. 86, 2016, pp. 20–27.

[71] Davis, P. J., and Rabinowitz, P., *Methods of numerical integration*, Courier Corporation, 2007.

[72] Li, K. S., and Lumb, P., "Reliability analysis by numerical integration and curve fitting," *Structural safety*, Vol. 3, No. 1, 1985, pp. 29–36.

[73] Lin, Y., "A quadrature-based technique for robust design with computer simulations," Ph.D. thesis, Massachusetts Institute of Technology, 2007.

[74] Rue, H., Martino, S., and Chopin, N., "Approximate Bayesian inference for latent Gaussian models by using integrated nested Laplace approximations," *Journal of the Royal Statistical Society Series B: Statistical Methodology*, Vol. 71, No. 2, 2009, pp. 319–392.

[75] Monahan, J. F., *Numerical methods of statistics*, Cambridge University Press, 2011.

[76] Oberkampf, W., Helton, J., and Sentz, K., "Mathematical representation of uncertainty," *19th AIAA applied aerodynamics conference*, 2001, p. 1645.

[77] Oberkampf, W., and Helton, J., "Investigation of evidence theory for engineering applications," *43rd AIAA/ASME/ASCE/AHS/ASC Structures, Structural Dynamics, and Materials Conference*, 2002, p. 1569.

[78] Casalino, D., Grande, E., Romani, G., Ragni, D., and Avallone, F., "Definition of a benchmark for low Reynolds number propeller aeroacoustics," *Aerospace Science and Technology*, Vol. 113, 2021, p. 106707.

[79] Drela, M., "XFOIL: An analysis and design system for low Reynolds number airfoils," *Low Reynolds number aerodynamics*, Springer, 1989, pp. 1–12.

[80] Montgomerie, B., "Methods for root effects, tip effects and extending the angle of attack range to±180, with application to aerodynamics for blades on wind turbines and propellers," *FOI, Swedish Defence Research Agency, Stockholm, Sweden, Report No. FOI*, 2004.

[81] Shubham, S., Ianakiev, A., and Wright, N., "Review of standalone small-scale Darrieus wind turbines - a Nottingham case study," *17th EAWE PhD Seminar on Wind Energy*, 2021.

[82] Shubham, S., Naik, K., Sachar, S., and Ianakiev, A., "Performance analysis of low Reynolds number vertical axis wind turbines using low-fidelity and mid-fidelity methods and wind conditions in the city of Nottingham," *Energy*, Vol. 279, 2023, p. 127904.

[83] Shubham, S., Wright, N., and Ianakiev, A., "Application of Richardson extrapolation method to aerodynamic and aeroacoustic characteristics of low Reynolds number vertical axis wind turbines," *28th AIAA/CEAS Aeroacoustics 2022 Conference*, 2022, p. 3022.

[84] Glegg, S., and Devenport, W., *Aeroacoustics of low Mach number flows: fundamentals, analysis, and measurement*, Academic Press, 2017.

[85] Avallone, F., Ragni, D., and Casalino, D., "On the effect of the tip-clearance ratio on the aeroacoustics of a diffuser-augmented wind turbine," *Renewable Energy*, Vol. 152, 2020, pp. 1317–1327.

[86] Lignarolo, L., Ragni, D., Scarano, F., Ferreira, C. S., and Van Bussel, G., "Tip-vortex instability and turbulent mixing in wind-turbine wakes," *Journal of Fluid Mechanics*, Vol. 781, 2015, pp. 467–493.



https://dspace.org/

Uncertainty propagation and management of mixed uncertainties for multi-fidelity multi-disciplinary analysis of propeller with different blade sweep

Shubham, Shubham; Kipouros, Timoleon; Dash, Siddhant; Ianakiev, Anton

2024-01-04
American Institute of Aeronautics and Astronautics (AIAA)
https://doi.org/10.2514/6.2024-1487
Shubham S, Kipouros T, Dash S, Ianakiev A. (2024) Uncertainty propagation and management of mixed uncertainties for multi-fidelity multi-disciplinary analysis of propeller with different blade sweep. In: AIAA SCITECH 2024 Forum, 8-12 January 2024, Orlando, USA, Paper number AIAA 2024-1487

Downloaded from a DSpace repository. https://dspace.org/